

# A non-stationary harmonic model for seasonal internal tide amplitude prediction

Matthew David Rayson<sup>1</sup>, Nicole L Jones<sup>1</sup>, Gregory N. Ivey<sup>1</sup>, and Yankun Gong<sup>1</sup>

<sup>1</sup>University of Western Australia

November 23, 2022

## Abstract

We present an empirical model for describing the temporal variability of the internal tide, that uses seasonal harmonics to temporally modulate the amplitude of the fundamental tidal harmonics. Internal tide data, from both long-term, in-situ moorings and a mesoscale- and internal tide-resolving ocean model, are used to demonstrate the performance of the seasonal (non-stationary) harmonic model for the Indo-Australian Basin Region. The non-stationary model described up to 15 % more baroclinic sea surface height and isotherm displacement variance than the fixed-amplitude harmonic model at some observation sites. The ocean model results demonstrate that the study region, which includes the Australian North West Shelf (NWS), Timor Sea and southern Indonesian Islands, is dominated by standing wave interference patterns produced by multiple generation sites. Application of the seasonal harmonic model demonstrates that temporal shifts in the standing wave locations coincide with seasonal variations in density stratification, particularly within 2 - 3 internal wave lengths from strong generation sites. It is shown that the variance fraction of internal tide signal explained by seasonal modulations is largest in standing wave node regions. This result helps explain the contrasting skill of the seasonal harmonic model at two moorings that were separated by only 38 km. Output of the harmonic model also demonstrates that the seasonally-evolving, southward propagating internal tide from Lombok Strait had a smaller amplitude in October when shear from the Indonesian Throughflow was strongest. Further applications for a regional internal tide climatology database are discussed.

# A non-stationary harmonic model for seasonal internal tide amplitude prediction

Matthew D. Rayson, Nicole L. Jones, Gregory N. Ivey, Yankun Gong

<sup>1</sup>Oceans Graduate School and The Oceans Institute, University of Western Australia

## Key Points:

- A new empirical model using seasonal harmonics is developed to characterise internal tide variability.
- Seasonal variations in standing internal tides from multiple sources lead to temporal modulations of individual harmonics.
- Internal tide predictability at a site is dependent on standing wave node locations.

---

Corresponding author: Matthew D. Rayson, [matt.rayson@uwa.edu.au](mailto:matt.rayson@uwa.edu.au)

**Abstract**

We present an empirical model for describing the temporal variability of the internal tide, that uses seasonal harmonics to temporally modulate the amplitude of the fundamental tidal harmonics. Internal tide data, from both long-term, in-situ moorings and a mesoscale- and internal tide-resolving ocean model, are used to demonstrate the performance of the seasonal (non-stationary) harmonic model for the Indo-Australian Basin Region. The non-stationary model described up to 15 % more baroclinic sea surface height and isotherm displacement variance than the fixed-amplitude harmonic model at some observation sites. The ocean model results demonstrate that the study region, which includes the Australian North West Shelf (NWS), Timor Sea and southern Indonesian Islands, is dominated by standing wave interference patterns produced by multiple generation sites. Application of the seasonal harmonic model demonstrates that temporal shifts in the standing wave locations coincide with seasonal variations in density stratification, particularly within 2 - 3 internal wave lengths from strong generation sites. It is shown that the variance fraction of internal tide signal explained by seasonal modulations is largest in standing wave node regions. This result helps explain the contrasting skill of the seasonal harmonic model at two moorings that were separated by only 38 km. Output of the harmonic model also demonstrates that the seasonally-evolving, southward propagating  $M_2$  internal tide from Lombok Strait had a smaller amplitude in October when shear from the Indonesian Throughflow was strongest. Further applications for a regional internal tide climatology database are discussed.

**Plain Language Summary**

Internal waves drive variability in ocean variables like sea surface height or internal water temperature throughout the ocean. In some regions, most of this variability is centered around the tidal frequencies, i.e., oscillating once or twice per day, due to the surface tides generating the waves. Surface tides are readily predictable using a technique called harmonic analysis due to the mechanical response of the ocean mass to gravitational pull from the Sun and Moon. Internal waves are forced by these tides, however, they are also influenced by temporally variable ocean conditions. Here, we modify the standard harmonic analysis method to account for seasonal variations in ocean properties. For some applications, internal wave-induced variability is considered to be noise

42 and therefore deterministic methods for describing their variability (the noise) are de-  
43 sirable.

## 44 1 Introduction

45 Prediction of internal tides - internal waves of tidal frequency - is important for nu-  
46 merous practical and ecological applications. Accurate prediction of internal tides is a  
47 crucial step in interpreting the future Surface Water Ocean Topography (SWOT) high-  
48 resolution altimetry mission and hence obtaining the submesoscale variability (Ray &  
49 Zaron, 2011; Arbic et al., 2015). Traditional satellite altimetry is unable to detect in-  
50 ternal tide-induced sea surface height (SSH) perturbations over continental shelves be-  
51 cause the horizontal wavelength of the barotropic tide is similar to the internal tide wave-  
52 length, making their extraction through wavenumber filtering difficult (Zaron, 2019). Hor-  
53 izontal instrument resolution is also a limitation in detecting the shorter internal tides  
54 on shelf regions (e.g. Ducet et al., 2000). For example, Zaron (2019)'s internal tide database  
55 (high-resolution empirical tide model, or, HRET) predicts internal tide SSH of less than  
56 1 cm in water depths between 200 and 500 m on the Australian North West Shelf (Fig  
57 1) - up to an order of magnitude smaller than observed. Predicting internal tides using  
58 other estimates besides altimetry-derived SSH predictions is therefore of critical impor-  
59 tance to the interpretation of SWOT SSH data in shelf and coastal zones.

60 Internal tide prediction techniques largely originate from surface tide methods, namely  
61 (stationary) harmonic analysis. Prediction of surface tides is either through empirical  
62 harmonic models with fixed tidal frequencies and spatially-varying harmonic amplitudes  
63 or response-based models (e.g., Munk & Cartwright, 1966; Foreman, 1977). The harmonic  
64 amplitudes are either estimated from tide gauge or satellite altimetry sea surface height  
65 data, or from solutions to the shallow-water equations (G. D. Egbert & Ray, 2017). A  
66 key characteristic of sites that are not predictable using this approach is that their spec-  
67 tral content exhibit broad "cusps" around each of the forcing frequencies instead of sin-  
68 gular spectral peaks (Munk & Cartwright, 1966). Broad spectral cusps are usually found  
69 in surface tide records where the tides undergo modulations due to low-frequency wa-  
70 ter level variations (e.g., from storm surge), changing bathymetry or nonlinear effects  
71 due to drag.

72 For internal tide records, broad spectral cusps, centered around the fundamental  
 73 tidal frequencies forced by the barotropic tide, seem to be the rule rather than the ex-  
 74 ception (e.g., Colosi & Munk, 2006). The frequency smearing is due to several processes,  
 75 including temporal variations in stratification and mesoscale flow (Ponte & Klein, 2015;  
 76 Buijsman et al., 2017; Rainville & Pinkel, 2006; Zaron & Egbert, 2014), and topographic  
 77 generation through interference from incoming waves (Kelly & Nash, 2010; Gong et al.,  
 78 2019). Given that they do not form sharp spectral peaks, internal tides are usually de-  
 79 fined as the band-passed portion of the signal of an ocean variable like water temper-  
 80 ature or buoyancy perturbation (Nash, Kelly, et al., 2012; Buijsman et al., 2017). It is  
 81 common to name the portion of the band-passed signal that can be modelled with fixed  
 82 tidal harmonics as the coherent internal tide, and the residual as the incoherent inter-  
 83 nal tide.

84 The incoherent internal tide is typically non-stationary and can comprise a signif-  
 85 icant portion of the total variance in some locations (Shriver et al., 2014; Nelson et al.,  
 86 2019). It is therefore desirable to model the part of the signal that cannot be explained  
 87 by fixed tidal frequencies. Zaron (2019) used the approach of Huess and Andersen (2001)  
 88 to account for seasonal variations in the  $M_2$  internal tide by including an annual mod-  
 89 ulation, and the non-stationary component is represented in the additional harmonics  
 90  $MA_2$  and  $MB_2$ . Here we extend this technique to other tidal frequencies and higher har-  
 91 monics. The purpose of this paper is to demonstrate that part of the non-stationary in-  
 92 ternal tide variance can be explained using a hierarchical harmonic fitting procedure that  
 93 accounts for seasonal amplitude modulations of the major tidal constituents (e.g.,  $M_2$ ,  
 94  $S_2$ ,  $K_1$ ,  $O_1$ ). We demonstrate the superior performance of this method, compared to the  
 95 harmonic method, using multi-year in situ mooring observations collected on the Aus-  
 96 tralian North West Shelf (NWS) and Timor Sea, and with a year-long 3D primitive equa-  
 97 tion ocean model solution encompassing the region.

98 The NWS, Timor Sea and Indonesian Archipelago are regions where large-amplitude  
 99 internal tides emanating from different generation sites interact and undergo seasonal  
 100 modulations (P. Holloway, 2001; Kelly et al., 2014; Robertson & Field, 2008; M. Rayson  
 101 et al., 2012; Gong et al., 2019). Nash, Shroyer, et al. (2012) in their assessment of 16 moor-  
 102 ing locations around the globe, found that the most coherent site was in the Timor Sea  
 103 (ITFTIS). Kelly et al. (2014), showed (by fitting harmonics to 30 day segment lengths)  
 104 that tidal harmonics at this site underwent annual modulations. They theorised that changes

105 in seasonal stratification, coherent on the length scale of the wave propagation distance  
 106 of a few hundred kilometers at this site, were responsible for the annual modulation of  
 107 the internal tide. We extend the Timor Sea mooring site fixed frequency (stationary) har-  
 108 monic model by allowing the amplitude of the major tidal harmonics to *slowly* vary in  
 109 time. We call this approach the non-stationary model as it allows for temporal modu-  
 110 lation of the harmonic amplitudes at the primary forcing frequencies (e.g.,  $M_2$ ,  $K_1$ ). This  
 111 approach requires specification of a model for the slowly-varying amplitudes, and here  
 112 we use observations from the Timor Sea mooring to justify using annual harmonics to  
 113 describe the temporal modulation.

114 The structure of this paper is as follows. In Section 2, we present the non-stationary  
 115 harmonic model and define several metrics for characterising the seasonality of internal  
 116 tides. Descriptions of the in situ data and numerical model setup are given in Section  
 117 3. Section 4 begins with an overview of the in situ observations before a quantitative eval-  
 118 uation of the non-stationary harmonic model is presented. We finish Section 4 with a  
 119 regional overview of the internal tide seasonality using the primitive equation ocean model  
 120 and explore potential physical drivers in the Discussion in Section 5. We conclude in Sec-  
 121 tion 6 with an overview of potential uses for an internal tide climatology data set and  
 122 potential modifications to the harmonic model.

## 123 **2 Non-stationary Harmonic Model**

124 Tidal variations in quantities such as internal wave amplitude,  $a$ , are typically mod-  
 125 eled using tidal harmonics by employing a series of sinusoidal basis functions with fixed  
 126 frequencies and amplitudes (cf. Foreman, 1977; G. D. Egbert & Ray, 2017)

$$a_i = \sum_m \alpha_m \cos(\omega_m t_i) + \beta_m \sin(\omega_m t_i) + \varepsilon, \quad (1)$$

127 where  $\omega_m$  are the tidal harmonic frequencies [cycles  $\text{d}^{-1}$ ],  $t_i$  is the time in days at step  
 128  $i$ ,  $\varepsilon$  is an error term, and  $\alpha_m$  and  $\beta_m$  are fixed amplitudes for each harmonic,  $m$ . Best  
 129 estimates of the amplitude parameters are typically found by linear least-squares fitting  
 130 to the time-series of  $a_i$ .

131 A non-stationary harmonic model is

$$a_i = \sum_m \alpha_{m,i} \cos(\omega_m t_i) + \beta_{m,i} \sin(\omega_m t_i) + \varepsilon_a, \quad (2)$$

132 where the key difference between Eq. 1 and Eq. 2 is that the amplitudes  $\alpha_{m,i}$  and  $\beta_{m,i}$   
 133 now vary with time. This approach, however, results in more unknown variables than  
 134 data points so the amplitude modulation must be parameterized.

135 Our non-stationary model allows the amplitudes to vary slowly in time using  $N$   
 136 seasonal harmonics. With the annual frequency  $\omega_A = 2\pi/365.25 \text{ d}^{-1}$ , the real and imag-  
 137 inary amplitudes are now

$$\alpha_{m,i} = \hat{\alpha}_{m,0} + \sum_{n=1}^N \hat{\alpha}_{m,n} \cos(n\omega_A t_i) + \hat{\beta}_{m,n} \sin(n\omega_A t_i), \quad (3)$$

138 and

$$\beta_{m,i} = \tilde{\alpha}_{m,0} + \sum_{n=1}^N \tilde{\alpha}_{m,n} \cos(n\omega_A t_i) + \tilde{\beta}_{m,n} \sin(n\omega_A t_i), \quad (4)$$

139 respectively. The complex time-varying amplitude for any tidal constituent,  $m$ , is

$$\hat{\eta}_{m,i} = \alpha_{m,i} + i\beta_{m,i}, \quad (5)$$

140 where  $i = \sqrt{-1}$ , and will be used throughout this paper to describe the internal tide  
 141 amplitude variability.

142 It is possible to estimate the unknown parameters in Eqs. (2) - (4) using linear least-  
 143 squares methods in two-steps. In the first step, short-time harmonic fits are used to es-  
 144 timate  $\alpha_{m,i}$  and  $\beta_{m,i}$  for discrete window periods, and in the second step the seasonal  
 145 harmonic amplitudes (parameters  $\hat{\alpha}$ ,  $\hat{\beta}$ ,  $\tilde{\alpha}$  and  $\tilde{\beta}$ ) are least-squares fit to the short-time  
 146 window amplitude used in step one. The down side of this approach is that one must  
 147 arbitrarily define a suitable window length. Alternatively, Eqs. (2) - (4) can be combined  
 148 to give

$$a_t = \sum_m \sum_{n=-N}^N A_{m,j} \cos([\omega_m + n\omega_A]t_i) + B_{m,j} \sin([\omega_m + n\omega_A]t_i) + \varepsilon_a, \quad (6)$$

149 where the subscript  $j = n+N+1$ . Eq. 6 highlights how the model captures a broader  
 150 spectrum of internal waves around each tidal forcing frequency through the additional  
 151 frequencies given by  $\omega_m \pm n\omega_A$ .

152 The unknown parameters which must be estimated from the observed data are the  
 153 amplitude matrices  $A_{m,j}$  and  $B_{m,j}$  that have  $M$  rows and  $2N+1$  columns. For exam-  
 154 ple, with 5 tidal constituents ( $M = 5$ ) and 3 annual harmonics ( $N = 3$ ),  $A_{m,j}$  and  
 155  $B_{m,j}$  each have 35 elements. Last, assuming the error term is zero-mean Gaussian white  
 156 noise, i.e.,  $\varepsilon_a \sim \mathcal{N}(0, \sigma_a^2)$ , the last parameter to estimate is the standard deviation of  
 157 the error term,  $\sigma_a$ . The practical benefit of writing the non-stationary model in the form

158 of Eq. 6 is that the parameters can be estimated in one step using linear least-squares  
 159 fitting. Seasonal modulation of the real and imaginary amplitudes of each tidal harmonic  
 160 (the terms in Eqs 3 and 4) are then back-calculated from the amplitude matrices in Eq.  
 161 (6) according to

$$\begin{aligned}
 \hat{\alpha}_{m,0} &= A_{m,N+1} \\
 \tilde{\alpha}_{m,0} &= B_{m,N+1} \\
 \hat{\alpha}_{m,n} &= A_{m,N-n+1} + A_{m,N+n+1} \\
 \hat{\beta}_{m,n} &= B_{m,N+n+1} - B_{m,N-n+1} \\
 \tilde{\alpha}_{m,n} &= B_{m,N-n+1} + B_{m,N+n+1} \\
 \tilde{\beta}_{m,n} &= A_{m,N-n+1} - A_{m,N+n+1}.
 \end{aligned} \tag{7}$$

162 Different metrics have been used in the literature to quantify the non-stationarity  
 163 of internal tides. Shriver et al. (2014) computed tidal fits to 183 30 d segments from 9  
 164 years of global HyCOM (numerical model) SSH data. They use the normalised RMS of  
 165 the amplitude for all 183 time blocks as a metric for non-stationarity. In their discus-  
 166 sion, they also fit annual harmonics to the amplitudes (their Fig. 11). Nash, Shroyer,  
 167 et al. (2012) used incoherence as a metric for non-stationarity. Their definition for co-  
 168 herence was the percentage of variance in the 6 - 30 hour band-pass filtered baroclinic  
 169 current records explained by fitting 8 tidal harmonics to 90 day segments. Ray and Zaron  
 170 (2011) fit tidal harmonics to altimetry data using data from specific months only to iden-  
 171 tify seasonality, and hence non-stationarity, of the tidal harmonics.

172 We define the following metrics to characterise the performance and frequency con-  
 173 tent of the non-stationary harmonic model. The total amount of variance fraction ex-  
 174 plained by the non-stationary harmonic fit (TVFH) is

$$TVFH = \frac{1}{2} \frac{\sum_{m=1}^5 \sum_{n=-3}^3 |\hat{A}_{m,j}|^2}{\langle SSH_{BC} \rangle^2}, \tag{8}$$

175 where  $\hat{A}_{m,j} = A_{m,j} + iB_{m,j}$ , and  $\langle SSH_{BC} \rangle^2$  is the total signal variance. A similar def-  
 176 inition also applies to the stationary harmonic model, which we call SVFH. These met-  
 177 rics define the performance of the harmonic model fit and are equivalent to a Murphy  
 178 Skill score (Murphy, 1988). The variance in an individual frequency band, including an-  
 179 nual harmonics, is

$$VF_m = \frac{\sum_{n=-3}^3 |\hat{A}_{m,j}|^2}{\sum_{m=1}^5 \sum_{n=-3}^3 |\hat{A}_{m,j}|^2}. \tag{9}$$

180 The last metric we included is the variance fraction of the non-stationary harmonics for  
 181 an individual frequency band, defined as

$$NSVF_m = 1 - \frac{|\hat{A}_{m,N+1}|^2}{\sum_{n=-3}^3 |\hat{A}_{m,j}|^2}. \quad (10)$$

182 These two metrics ( $VF_m$  and  $NSVF_m$ ) explain the dominance of a particular harmonic  
 183 to the total internal tide signal, and the importance of seasonal modulation to that par-  
 184 ticular harmonic, respectively.

### 185 3 Methods

#### 186 3.1 *In situ* mooring data

187 Long time-series of two internal tide ocean quantities, namely the internal mode  
 188 amplitude,  $a$ , and the baroclinic sea surface height perturbation,  $SSH_{BC}$ , were extracted  
 189 from water temperature observations from four vertical moorings deployed in water depths  
 190 greater than 200 m along the outer region of the Australian North West Shelf and Timor  
 191 Sea (Fig. 1). Moorings were deployed as part of the Australian Integrated Marine Ob-  
 192 serving System (IMOS), with the first deployment in February 2012 and the last retrieval  
 193 in August 2014. Servicing was conducted roughly every six months. Each mooring was  
 194 equipped with Seabird 37/39/56 thermistors that measured water temperature at 60 s  
 195 intervals. Instruments were nominally spaced at 20 m depth increments with the upper-  
 196 most thermistor located 20 - 30 m below mean sea level (Tab. 1). Data from an addi-  
 197 tional three IMOS moorings that collected TWC temperature data from Aug 2019 - Feb  
 198 2020 were used as additional validation data.

##### 199 3.1.1 *Internal tide amplitude estimation*

200 The steps to go from water temperature,  $T_{k,i}$  measured with fixed vertical moor-  
 201 ings at discrete vertical heights, subscript  $k$ , at time interval  $i$ , to band-passed internal  
 202 tide amplitude,  $a_i$ , are as follows.

- 203 1. Convert temperature to density using a nonlinear equation of state with the cli-  
 204 matological mean salinity at each site (34.6 psu).
- 205 2. Decompose density into a background component and a perturbation component

$$\rho_{k,i} = \langle \rho \rangle_{k,i} + \rho'_{k,i}$$

206 where the background component,  $\langle \rho \rangle_{k,i}$ , is low-pass filtered to remove tidal and  
 207 higher frequencies (we use a 2-day moving average).

208 3. Compute the full-water-column background density profile from the discrete data  
 209 by fitting it to a continuous function

$$\langle \rho \rangle_i(z) = \beta_0 - \beta_1 \left[ \tanh \left( \frac{z + \beta_2}{\beta_3} \right) + \tanh \left( \frac{z + \beta_4}{\beta_5} \right) \right]$$

210 4. Calculate the buoyancy frequency,  $N$ , and the vertical mode structure functions,  
 211  $\phi_j$  for each vertical mode  $j$  from the full-water-column background density where

$$N^2(z) = -\frac{g}{\rho_0} \frac{d\langle \rho \rangle}{dz}$$

212  $g = 9.81 \text{ m s}^{-2}$  is the acceleration due to gravity and  $\rho_0 = 1024 \text{ kg m}^{-3}$  is a  
 213 reference density. The vertical structure functions are then determined from the  
 214 normal mode eigenvalue equation

$$\frac{d^2 \phi_i}{dz^2} + \frac{N_i^2}{c_i^2} \phi = 0 \tag{11}$$

215 subject to boundary conditions at the top and bottom  $\phi(0) = \phi(-H) = 0$ , re-  
 216 spectively. The eigenvalues,  $c$ , are the long-wave phase speed assuming zero ro-  
 217 tation.

218 5. Define buoyancy perturbations as  $b(z, t) = -g\rho'(z, t)/\rho_0$  and solve

$$b(z, t) = \sum_{j=1}^4 A_j(t) N^2(z) \phi_j(z),$$

219 using least-squares to get a time-series of buoyancy-perturbation amplitude,  $A_j(t)$ ,  
 220 for each vertical mode.

221 6. Decompose the amplitude into an internal tide component and a residual

$$A_j(t) = a_j(t) + A'_j(t)$$

222 where  $a_j(t)$  is defined as the band-pass filtered component where we used a But-  
 223 terworth filter with 6 and 33 hour cutoff periods. It is the internal tide compo-  
 224 nent  $a_j(t)$  that we seek to describe with the non-stationary harmonic model.

### 225 **3.1.2 Baroclinic sea surface height estimation**

226 The internal tide-induced perturbation of the free-surface, the baroclinic sea sur-  
 227 face height ( $SSH_{BC}$ ), is (Zhao et al., 2016)

$$SSH_{BC} = \frac{p_{surf}}{\rho_0 g} \tag{12}$$

228 where

$$p_{surf} = \rho_0 \int_{-H}^0 b \, dz,$$

229 is the surface pressure perturbation,  $\rho_0 = 1024 \text{ kg m}^{-3}$  is a constant reference density,  
 230  $H$  is the water depth, and  $b$  is the buoyancy perturbation about the background den-  
 231 sity i.e.,

$$b = -\frac{(\rho - \langle \rho \rangle)g}{\rho_0}.$$

232 Note that the definition in Eq. 12 is related to the steric height definition of Savage  
 233 et al. (2017), but with a few subtle differences. Using our notation, Savage et al. (2017)  
 234 calculate the steric height  $\eta_s$  from a primitive equation ocean model (HYCOM) via

$$\eta_s = \frac{\overline{\langle \rho \rangle}}{\bar{\rho}} \eta_0 + \frac{\overline{\langle \rho \rangle} - \bar{\rho}}{\bar{\rho}} H$$

235 where  $\overline{(\ )}$  denotes a depth-averaged quantity and  $\eta_0$  is the initial steric height. Eq. 12 can  
 236 be re-written in this form to give

$$SSH_{BC} = \frac{\overline{\langle \rho \rangle} - \bar{\rho}}{\rho_0} H.$$

237 The key points of difference are that we use a reference density in the denominator, as-  
 238 sume  $\eta_0 = 0$  and use a different definition for the background density  $\langle \rho \rangle$ . Savage et  
 239 al. (2017) were interested in the steric height at all frequencies so used a long-term av-  
 240 erage. Conversely, as we are interested in tidal frequency perturbations to the free-surface,  
 241 we used a low-pass filter with a cutoff period of 60 hours to give  $\langle \rho \rangle$ .

## 242 **3.2 SUNTANS Model**

### 243 **3.2.1 Motivation**

244 A realistic three-dimensional primitive equation ocean solver (described below) was  
 245 used to model the basin-scale ocean circulation (with tides) for a 12-month period. The  
 246 purpose of the ocean model was to capture the seasonal variations in large-scale circu-  
 247 lation, stratification and their influence on the internal tides. The Indo-Australian basin  
 248 and the surrounding shelf seas and island chains were investigated in detail; it is one ex-  
 249 ample of many global regions where large scale flow is likely to influence temporal vari-  
 250 ability of internal tides, which propagate from many different topographic generation re-  
 251 gions.

### 3.2.2 Governing equations

We employ the hydrostatic version of the unstructured grid Stanford University Nonhydrostatic Terrain-following Adaptive Navier-Stokes (SUNTANS) solver (Fringer et al., 2006) to model the ocean circulation. The model solves the Reynolds-averaged Navier-Stokes equations with the Boussinesq and hydrostatic approximations,

$$\frac{\partial u}{\partial t} + \nabla \cdot (\mathbf{u}u) - fv = -g \frac{\partial}{\partial x} (\eta + r) + \nabla_H \cdot (\nu_H \nabla u) + \frac{\partial}{\partial z} \left( \nu_v \frac{\partial u}{\partial z} \right), \quad (13)$$

$$\frac{\partial v}{\partial t} + \nabla \cdot (\mathbf{u}v) + fu = -g \frac{\partial}{\partial y} (\eta + r) + \nabla_H \cdot (\nu_H \nabla v) + \frac{\partial}{\partial z} \left( \nu_v \frac{\partial v}{\partial z} \right), \quad (14)$$

where  $\nabla = (\partial/\partial x, \partial/\partial y, \partial/\partial z)$ ,  $\mathbf{u} = (u, v, w)$  are the eastward, northward and vertical velocity components, respectively,  $f$  is the Coriolis frequency, and  $\nu_H$  and  $\nu_v$  are the horizontal and vertical eddy viscosity. The free surface elevation is  $\eta$  and  $r$  is the baroclinic pressure head given by

$$r = \frac{1}{\rho_0} \int_z^\eta \rho \, dz.$$

where  $\rho_0$  is the reference density ( $1000 \text{ kg m}^{-3}$ ), and  $\rho$  is a perturbation density. The continuity equation is

$$\nabla \cdot \mathbf{u} = 0,$$

and the free surface,  $\eta$ , is updated by solving the depth-integrated continuity equation

$$\frac{\partial \eta}{\partial t} + \frac{\partial}{\partial x} \left( \int_{-H}^\eta u \, dz \right) + \frac{\partial}{\partial y} \left( \int_{-H}^\eta v \, dz \right) = 0.$$

The tracer (temperature and salinity) transport equations are

$$\frac{\partial T}{\partial t} + \nabla \cdot (\mathbf{u}T) = \frac{\partial}{\partial z} \left( K_T \frac{\partial T}{\partial z} \right) + \frac{\partial Q_{sw}}{\partial z}$$

$$\frac{\partial S}{\partial t} + \nabla \cdot (\mathbf{u}S) = \frac{\partial}{\partial z} \left( K_S \frac{\partial S}{\partial z} \right)$$

where  $T$  is the temperature [ $^{\circ}\text{C}$ ],  $S$  is the salinity,  $K_T$  and  $K_S$  are the vertical temperature and salinity diffusivity [ $\text{m}^2 \text{ s}^{-1}$ ], and  $Q_{sw}$  is the penetrative shortwave radiation flux, [ $^{\circ}\text{C m s}^{-1}$ ]. A nonlinear equation of state is used to relate density  $\rho$  to  $T$ ,  $S$  and pressure [REF].

The model equations are discretized using a hexagonal dominant unstructured horizontal grid (see M. Rayson et al. (2018)) with fixed-height vertical ( $z$ -layer) coordinates. See M. D. Rayson et al. (2015) for a thorough overview of the model surface heat, salt and momentum boundary conditions, and Fringer et al. (2006) for an overview of the model discretization and numerical solution method.

276 **3.2.3 Model parameterizations**

277 The surface,  $z = \eta(x, y, t)$ , and seabed,  $z = -H(x, y)$ , boundary conditions of  
 278 the horizontal momentum equations (13, 14) are

$$\nu_v \frac{\partial \mathbf{u}}{\partial z} \Big|_{z=\eta} = \frac{\vec{\tau}_s}{\rho_0}$$

$$\nu_v \frac{\partial \mathbf{u}}{\partial z} \Big|_{z=-H} = \frac{\vec{\tau}_b}{\rho_0}$$

279 where  $\vec{\tau}_s = (\tau_{x,s}, \tau_{y,s})$  and  $\vec{\tau}_b = (\tau_{x,b}, \tau_{y,b})$  are the surface and seabed stress compo-  
 280 nents, respectively. The surface stress is parameterized by

$$\vec{\tau}_s = C_{da} \rho_a |\mathbf{U}_a| (\mathbf{U}_a - \mathbf{u}|_{z=\eta})$$

281 where  $\rho_a$  is the density of air ( $1.2 \text{ kg m}^{-3}$ ),  $\mathbf{U}_a$  is the horizontal wind velocity vector,  
 282 and  $C_{da}$  is the empirical surface drag coefficient. A quadratic drag formulation was also  
 283 used to define the seabed stress

$$\vec{\tau}_b = -\rho_0 C_d |\mathbf{u}|_{z=-H} \mathbf{u}|_{z=-H}.$$

284 We used a quadratic bed drag coefficient of  $C_d = 0.002$ . The surface drag coefficient  
 285 was calculated using the COARE 3.0 algorithm (Fairall et al., 2003), which is wind speed  
 286 dependent. The horizontal eddy viscosity was constant ( $\nu_H = 1.0 \text{ m}^2 \text{ s}^{-1}$ ) and the ver-  
 287 tical eddy viscosity and tracer diffusivities were computed with the Mellor and Yamada  
 288 (1982) turbulence closure scheme.

289 **3.2.4 Grid**

290 The model domain encompassed the Australian North West Shelf, Timor Sea and  
 291 the southern Indonesian Archipelago because these are all known internal wave gener-  
 292 ation regions. The meridional span of the grid was  $23^\circ \text{ S}$  to  $5^\circ \text{ S}$  and the zonal span  
 293 was  $108^\circ \text{ E}$  (west of Western Australia) to  $145^\circ \text{ E}$ . The easternmost boundary was set  
 294 to the shallow (20 m) Torres Strait off northern Queensland where there is limited vol-  
 295 ume exchange with the Coral Sea relative to the Indonesian Throughflow.

296 SUNTANS uses a finite-volume discretization of the governing equations and there-  
 297 fore employs an unstructured horizontal grid (Fig. 2). We used a hexagonal-dominant

298 grid that had the finest resolution (roughly 2 km) over the North West Shelf and 4 km  
299 resolution in the Timor Sea and the major Indonesian passages of Timor, Ombai and  
300 Lombok Straits (Fig 2b). The horizontal resolution telescoped out to about 10 km along  
301 all of the open boundaries, coinciding with the resolution of the ocean model used to force  
302 the model at the open boundaries (described below). The total number of horizontal grid  
303 cells was 225,368. The unstructured grid can therefore efficiently span a large domain  
304 with the ability to focus resolution around a region of interest, namely the North West  
305 Shelf and the Indonesian-Australian Basin. Grid coordinates were projected in the World  
306 Mercator projection (EPSG 54004; <https://epsg.io/54004>) in order to perform metric  
307 distance calculations.

308 The vertical grid consisted of 80 layers with logarithmic stretching from the sur-  
309 face down to the deepest depth (capped at 6000 m). The vertical resolution was roughly  
310 7 m for the surface layer and each layer thickness increased on the last by a factor of 1.045,  
311 giving approximately 20 layers in the upper 250 m and a vertical resolution of roughly  
312 200 m in the abyssal ocean.

313 A new gridded bathymetry dataset was compiled for the NWS and Indonesian Seas  
314 from several data sets using a similar blending method to that described in M. D. Rayson  
315 et al. (2017). The input data sets were the Geoscience Australia (GA) 250 m grid from  
316 2009, 50 m resolution multibeam data provided by GA and high-resolution multibeam  
317 data provided by Woodside Energy Ltd in selected regions over the NWS. The key dif-  
318 ference in this study is that the General Bathymetric Chart of the Oceans (GEBCO) global  
319 30 arc second grid was used in the Indonesian Seas outside of the GA 250 m grid domain.  
320 Gridded bathymetry data were interpolated onto the unstructured grid cell centres (Fig.  
321 2a), and the maximum depth was capped at 6000 m.

### 322 ***3.2.5 Model Boundary and Initial Conditions***

323 Background ocean state variables used for the SUNTANS initial and boundary con-  
324 ditions were sourced from the Mercator Ocean global reanalysis product, GLORYSv2.  
325 We used daily-average temperature, salinity and velocity variables and interpolated them  
326 in space and time onto our model grid points. The GLORYS reanalysis uses the NEMO  
327 ocean model with a 1/12th degree resolution global grid and 50 vertical z-levels. The model  
328 assimilates satellite sea surface height and temperature data, as well as in situ data from

329 ARGO profilers, moorings and other sources. It is forced at the ocean surface by the ERA-  
 330 interim atmospheric reanalysis product (described below).

331 Barotropic tidal velocity and free-surface boundary conditions were derived from  
 332 the OTIS China and Indonesian Seas regional tide solution (G. Egbert & Erofeeva, 2002).  
 333 This regional tide solution has finer grid resolution ( $1/30^\circ$ ) than the global solution ( $1/4^\circ$ )  
 334 and is therefore able to resolve the Indonesian Archipelago topography in greater detail  
 335 to provide better tidal predictions (Stammer et al., 2014). Time-varying velocity fluxes  
 336 and free-surface elevations were reconstructed from eight tidal constituents, namely  $M_2$ ,  
 337  $S_2$ ,  $N_2$ ,  $K_2$ ,  $K_1$ ,  $O_1$ ,  $P_1$ ,  $Q_1$ , at the SUNTANS open boundary edges. Tidal fluxes were  
 338 added to the low-frequency (daily-average) open boundary velocities interpolated from  
 339 the GLORYS reanalysis.

340 Atmospheric data from the European Centre for Medium Range Weather Forecast’s  
 341 (ECMWF) ERA-Interim climate reanalysis product was used to drive the exchange of  
 342 momentum and heat between the atmosphere and the model ocean. ERA-Interim is a  
 343 global, data-assimilating atmospheric hindcast model run on a roughly 100 km grid with  
 344 output data stored at six-hourly time steps (Dee et al., 2011). Air-sea fluxes are param-  
 345 eterized in SUNTANS using the COARE3.0 algorithm using east- and north-wind ve-  
 346 locity referenced to 10 m above the surface, air temperature, pressure, and relative hu-  
 347 midity (Fairall et al., 2003). Net longwave and shortwave radiation components are cal-  
 348 culated internally within the model using cloud cover from ERA-Interim and model lat-  
 349 itude and time to compute the solar input (see M. D. Rayson et al. (2015) for a descrip-  
 350 tion of the numerical implementation of the heat flux module in SUNTANS).

### 351 **3.3 Validation**

352 We first tested the performance of the ocean model to reproduce the low-frequency  
 353 evolution of the temperature stratification on the shelf by comparison with through-water-  
 354 column temperature at the four different shelf locations. Model variables were saved at  
 355 the observation sites with the same temporal sampling interval (60 seconds). We then  
 356 linearly interpolated model data onto the observation depths. Temperature bias and RMSE  
 357 was computed for three different months to evaluate the model performance at captur-  
 358 ing the seasonal surface layer and thermocline variations over the region. At the ITFTIS  
 359 mooring, the model did well at replicating the surface heating and cooling from Septem-

ber 2013 to June 2014, as well as the mixed layer deepening in June (Fig 3). Bias in the upper 100 m was generally close to zero and the RMSE was  $< 0.5$  °C. Model performance was generally worse in the thermocline between 100 and 300 m deep. At the ITFTIS mooring, the model exhibited a 1 - 3 °C warm bias that was most pronounced during June 2014. RMSE was also higher in the thermocline where there were large high-frequency temperature variations due to internal tides. Higher RMSE at these depths were therefore reflective of both mean and internal tide-induced model-data mismatch. Note that as the model was unable to resolve high-frequency, nonlinear internal waves that were present in the observations this also contributed to higher RMSE.

Equivalent model temperature validation plots for the PIL200, KIM400 and KIM200 sites are included in the Supplementary Material. Bias was generally less at the PIL200 and KIM200 shelf sites ( $\pm 1$  °C), while at the KIM400 site the model exhibited a 1 - 3 °C cool bias in the thermocline between 100 and 300 m. This indicated that there was no systematic temperature bias in the model and that any biases were regionally specific. Poorer validation statistics in the thermocline were due to 20 - 50 m offset in the thermocline depths and admittedly, there is room for improvement in this aspect. Accurately capturing the thermocline structure and strength, however, is an on-going major challenge for all ocean/climate models (e.g., Castaño-Tierno et al., 2018). Overall, the model performed well at capturing the seasonal evolution of near-surface temperature and mixed layer development at each site. It also captured seasonal fluctuations in thermocline strength and width - the main ocean properties likely to temporally modulate internal tides on a regional scale.

## 4 Results

### 4.1 Non-stationary internal tides in the Timor Sea

Seasonal variability of the internal tide is exemplified in the  $SSH_{BC}$  signal observed at the Timor Sea (ITFTIS) mooring. Short-time harmonic fits of 5 major tidal constituents to 30-day segments over three years revealed seasonal oscillations in the dominant  $K_1$  frequency at the site (Fig. 4a). The  $K_1$  harmonic, in particular, had a strong semi-annual ( $2\omega_A$ ) cycle that could even be noticed in the raw data. Fits of the first three annual harmonics to short time fit harmonic amplitudes are also shown in Fig 4a. These are the slowly-varying real and complex amplitudes ( $\alpha_{m,i}$  and  $\beta_{m,i}$ ) in Eqs. 3 and 4. Eq. 6 shows

391 the relationship between the annual harmonics and the spectral content of the signal.  
 392 Annual harmonics have an equivalent frequency offset by  $\pm n\omega_A$  from each tidal frequency  
 393 and, since we use  $N = 3$  harmonics, there are 6 additional spectral bands per tidal con-  
 394 stituent (Fig 4b and c). For example, the semi-annual peak in  $K_1$  amplitude (i.e.,  $K_1 +$   
 395  $2\omega_A$ ) was evident in the discrete Fourier transform (DFT) amplitude at ITFTIS where  
 396 its amplitude was roughly 40 % of the primary frequency (Fig 4b). The semi-diurnal am-  
 397 plitude harmonics were about an order of magnitude smaller than the diurnal harmon-  
 398 ics at the ITFTIS and the DFT highlighted that the  $M_2$  band was broadly distributed  
 399 with amplitude peaks at various annual harmonics (Fig. 4c). Based on this site, we demon-  
 400 strate the effectiveness of the non-stationary model to capture internal tide seasonal vari-  
 401 ations. While not all annual harmonics were significant at ITFTIS, their inclusion gives  
 402 the model suitable flexibility to be broadly applicable to other sites. We will demonstrate  
 403 the suitability of the approach throughout this paper.

#### 404 **4.2 Non-stationary harmonic model evaluation**

405 We performed the following comparisons of the empirical harmonic models (sta-  
 406 tionary and non-stationary) using the following in situ variables:

- 407 • Mode-1 amplitude at four IMOS moorings (PIL200, KIM200, KIM400, ITFTIS)  
 408 for a multi-year period (Apr 2012 - Sep 2014);
- 409 •  $SSH_{BC}$  at the same four IMOS moorings for the 12-month model period (July  
 410 2013 - July 2014);
- 411 •  $SSH_{BC}$  at the same four IMOS moorings for a 12-month period outside of the orig-  
 412 inal numerical model period that was used to estimate the harmonic parameters  
 413 (July 2012 - July 2013).

414 We focused on two internal wave-induced ocean state variables to test the harmonic pre-  
 415 dictions. The first variable was the mode-1 buoyancy perturbation amplitude, and the  
 416 second was the baroclinic sea surface height. Buoyancy amplitude was chosen as it iso-  
 417 lates the signal from individual modes, while  $SSH_{BC}$  is a more practical variable because  
 418 it can be measured from space using altimetry. Note that  $SSH_{BC}$  also acts like a filter  
 419 in that the SSH response is inversely proportional to the vertical mode number so the  
 420 majority of the signal variance is due to the first baroclinic mode (Zaron 2011). It also  
 421 allows comparison of our model with other studies which have focused on sea surface height

(e.g., Zhao et al., 2016; Zaron, 2019; Savage et al., 2017; Nelson et al., 2019; Shriver et al., 2014).

We used the non-stationary harmonic amplitudes to characterise the seasonal and geographic variability of different tidal constituents at each site. Following these comparisons, we used the 3D primitive equation solution to make predictions of  $SSH_{BC}$  at the mooring locations over the same period when the model was run (July 2013 - June 2014). We then used the ocean model to make predictions at other observational sites collected during different years to the model run period. Last, the ocean model results were used to interpret the seasonal and geographic variability of the in situ observations. Throughout the paper, we use the skill score as a performance evaluation metric

$$skill = 1 - \frac{\sum(X_{mod} - X_{obs})^2}{\sum(X_{obs} - \mu_{obs})^2},$$

where  $X_{obs}$  and  $X_{mod}$  are the observed and model quantities, respectively, and  $\mu_{obs}$  is the mean observed quantity.

#### 4.2.1 Mode-1 Amplitude

The total mode-1 amplitude variability, as measured by the standard deviation of raw  $a$  for 60-s intervals, was largest at the PIL200 and ITFTIS site (7.1 and 7.3 m, respectively) (Table 2). The standard deviation of KIM400 was roughly half of KIM200, despite the moorings being 38 km apart. This is attributable to the KIM400 mooring being near a standing wave node (e.g., Rayson, 2012), an important result that we will demonstrate later when we show the geographic internal tide variability from the year-long ocean model simulation.

Another feature of the internal wave variability at each of the four sites was that only 20 - 30 % of the amplitude variance was contained within a period range of 6 - 34 hours (broadly encompassing the tidal bands), with the ITFTIS site being the exception with 50 % of the variance contained within these bands. The total variance in the 3 - 34 hour band was much larger (70 - 80 %) at all sites. This larger amount of variance in the super-tidal frequencies at all sites was likely due to the nonlinear steepening of internal tides. Each mooring was located at or near the edge of the continental shelf in water depths of 200 - 500 m, a depth range where the internal tides are known to undergo nonlinear steepening (P. Holloway et al., 1997; Grimshaw et al., 2006; M. D. Rayson et al., 2019).

452 We tested the suitability of the two empirical harmonic models by comparing the  
 453 baroclinic mode-1 amplitude,  $a$  with the in situ data from four IMOS moorings that were  
 454 deployed between 2012 and 2014. For the mode-1 amplitude at the ITFTIS and KIM200  
 455 sites, the skill of the non-stationary harmonic model was greater at all four sites (Ta-  
 456 ble 3): the non-stationary harmonic model had a skill of 0.78 and 0.81, respectively, while  
 457 the stationary harmonic model had a skill of 0.66 and 0.70, respectively. The skill of both  
 458 harmonic models was smallest at KIM400 and PIL200, although the non-stationary model  
 459 skill was still greater.

#### 460 **4.2.2 Baroclinic SSH**

461 We compared the  $SSH_{BC}$  for two time periods. The first was July 2013 - June 2014  
 462 and represents the period used to estimate the harmonic amplitude parameters for both  
 463 the stationary (Eq. 1) and non-stationary (Eq. 6) models; it is therefore a training pe-  
 464 riod. The second period was July 2012 - July 2013 when no data was used to estimate  
 465 model parameters and hence was a more robust test of the predictive skill of each har-  
 466 monic model.

467 The performance of the non-stationary model in predicting  $a$  was similar for pre-  
 468 dicting  $SSH_{BC}$  at each of the four sites (Table 4). The non-stationary model had a skill  
 469 score of 0.88 at ITFTIS compared with 0.78 for the stationary model (Fig. 5). This was  
 470 the best performing site followed by KIM200 (skill=0.69), PIL200 (skill=0.45) and KIM400  
 471 (0.41). The skill score increased and the RMSE reduced at all sites with the non-stationary  
 472 model, indicating that it is a better performing model, at least for the period contain-  
 473 ing the data used to estimate the coefficients. The skill at PIL200 and KIM400 showed  
 474 roughly 50 % improvement by switching to the non-stationary model, suggesting that  
 475 a larger amount of the variance at the site was explained by the seasonal modulation of  
 476 the  $M_2$  constituent (discussed below).

477 To further test the veracity of the non-stationary model, we extrapolated the  $SSH_{BC}$   
 478 to the period of July 2012 - June 2013 (the previous 12-months of observation data) and  
 479 calculated the model performance metrics (Table 5). For this period, both the skill and  
 480 RMSE were similar between the two harmonic models at all sites. For example, at ITFTIS  
 481 the skill was 0.75 and 0.76 for the stationary and non-stationary model, respectively. This  
 482 result suggests that the current non-stationary model was less suitable when applied to

483 a time period outside of the parameter training period, and that inter-annual variabil-  
 484 ity is likely important. However, the data at the ITFTIS site showed that the non-stationary  
 485 model was qualitatively detecting the semi-annual increase in  $SSH_{BC}$  (not shown). There  
 486 was a slight phase offset and this resulted in a large error for this year of data (July 2012  
 487 - June 2013) and this error was reflected in the skill score calculated over 12-months (Ta-  
 488 ble 5). This result of a phase shift in the semi-annual modulation indicates inter-annual  
 489 variability is likely important, which we have not accounted for at present.

#### 490 **4.2.3 SUNTANS SSH Validation**

491 We tested the ability of the 3D primitive equation ocean model to capture the re-  
 492 gional internal tide dynamics by making predictions of  $SSH_{BC}$  using the non-stationary  
 493 harmonic parameters derived from the SUNTANS solution. This enabled a comparison  
 494 between sites that had concurrent data collection with the model run period (ITFTIS,  
 495 KIM200, KIM400 and PIL200) and observations collected outside of this period (NWS-  
 496 BAR, NWSROW and NWSBRW moorings). Note that here we are comparing results  
 497 with the band-passed filtered observation data, not the harmonically-reconstructed ob-  
 498 servation data. At most sites, the skill score was greater than zero, indicating some pre-  
 499 dictive capability of the SUNTANS-derived harmonic model (Table 6). The best predic-  
 500 tions were (in descending order) the NWSBRW, NWSROW and ITFTIS sites (Skill of  
 501 0.67, 0.45 and 0.47, respectively). Note that these were also generally regions of larger  
 502 total internal tide amplitude (as will be shown below). The poorest predictions were at  
 503 the KIM400, PIL200 and NWSBAR sites with skill scores of -0.60, 0.02 and 0.12, respec-  
 504 tively. These results indicate poorer predictive skill of the non-stationary harmonic model  
 505 (and SUNTANS) along the southern (Pilbara) section of the NWS.

#### 506 **4.2.4 Seasonal modulation of the internal tide harmonics**

507 Seasonal  $SSH_{BC}$  complex harmonic amplitude,  $|\hat{\eta}_m(t)|$  (Eq. 5), of the five tidal  
 508 bands at each of the four sites revealed variable seasonal oscillations in the internal tide  
 509 harmonics (Fig 6). At ITFTIS (described earlier in Fig. 4), the  $K_1$  and  $O_1$  harmonics  
 510 had a strong semi-annual cycle although were out of phase;  $K_1$  peaked in July and Jan-  
 511 uary while  $O_1$  peaked in November and April (Fig. 6a). The SUNTANS model best re-  
 512 produced the seasonal variability at the ITFTIS site. The model captured the semi-annual  
 513 oscillations in the  $K_1$  internal tide ( $|\eta_{K1}(t)|$ ) although was 15 % weaker in magnitude.

514 Seasonal variations in other constituents at this site were in poorer agreement although  
 515 all had similar mean amplitudes.

516 At KIM200 (the next most predictable site), the dominant  $M_2$  harmonic had a tri-  
 517 annual peak and was largest in August, January and May (Fig 6b). The other four tidal  
 518 frequencies were all about 25 % or more smaller in magnitude except for  $K_1$ , which had  
 519 tri-annual peaks that were roughly 50 % of the  $M_2$  amplitude. The  $K_1$  tri-annual sig-  
 520 nal was also apparent in the SUNTANS model although two of the peaks were 50 % weaker.  
 521 At the nearby KIM400 mooring (38 km away), the  $M_2$  band was at least 25 % of the mag-  
 522 nitude of KIM200 and the  $K_1$  internal tide was dominant (Fig. 6c). The  $K_1$  harmonic,  
 523 however, had a different seasonal structure between the two sites. SUNTANS predicted  
 524 a dominant  $M_2$  component although  $K_1$  was dominant in the observations (Fig 6c). Again  
 525 the model under-predicted  $K_1$  by about 50 %. The model was, however, in agreement  
 526 that the KIM400 semi-diurnal components were significantly weaker than at KIM200.

527 The seasonal oscillations of the internal tide harmonics exhibited the most com-  
 528 plex behaviour at the PIL200 site (Fig. 6d). The  $M_2$  and  $K_1$  bands were dominant al-  
 529 though their relative importance varied significantly throughout the year. The  $M_2$  band  
 530 had tri-annual peaks in July, October and March, while the  $K_1$  band had a semi-annual  
 531 cycle with peak amplitude in December and July. This resulted in  $K_1$  dominating at PIL200  
 532 between October and February and  $M_2$  dominating for the other times of the year. The  
 533 exception being September, when  $M_2$ ,  $N_2$  and  $K_1$  were of equal magnitude. The non-  
 534 stationary harmonic model performed poorest at PIL200, likely the result of transient  
 535 dynamics not being captured by fitting annual harmonics. At PIL200, the SUNTANS  
 536 model was in qualitative agreement in terms of the seasonal evolution of the semi-diurnal  
 537  $SSH_{BC}$  components.

538 Generally, the SUNTANS derived internal tides were weaker in magnitude when  
 539 compared to the observed major constituents at all sites. The exception being at KIM400  
 540 (Fig 6c). Given the strength of the barotropic tidal forcing was skillfully captured by the  
 541 model, we suggest that the weaker modeled internal tides were due to a combination of  
 542 effects: biases in the mean thermocline properties; errors in bathymetry; discretization-  
 543 induced numerical dissipation due to insufficient horizontal resolution; and too much pa-  
 544 rameterized dissipation.

545 **4.2.5 Summary of observations**

546 The key insights gained from the empirical harmonic analysis of the in situ moor-  
 547 ing data at four locations along the shelf were:

- 548 • Internal tide predictability using either fixed amplitude (stationary) harmonics or  
 549 time-varying (non-stationary) harmonics was best explained at the ITFTIS and  
 550 KIM200 sites.
- 551 • Internal tides at all of the sites were predicted better using the non-stationary har-  
 552 monic model i.e., accounting for seasonal variability.
- 553 • The non-stationary model performed similarly to the stationary model when ap-  
 554 plied to data from a different time period than that used for harmonic fitting, im-  
 555 plying that inter-annual variability of harmonics was also an important factor.
- 556 • Internal tide amplitude  $a$  was more predictable than  $SSH_{BC}$  in terms of skill, prob-  
 557 ably because  $a$  only contains mode-1 contributions.
- 558 • ITFTIS was previously shown by (Nash, Shroyer, et al., 2012) to be the most pre-  
 559 dictable (in terms of a harmonic fit to a 90 day data segment) site of the 16 global  
 560 shelf moorings investigated. Here we show that the dominant  $K_1$  amplitude has  
 561 a semi-annual modulation at this site.
- 562 • KIM400 had roughly 50 % smaller amplitude internal tides than KIM200 despite  
 563 being located only 38 km away.
- 564 • PIL200 had poor predictability and complicated seasonal variability, such as the  
 565 dominance of different harmonics throughout the year.

566 We now use the numerical model results to further explore potential reasons for the ge-  
 567 ographic variability in seasonal internal tide variability that was observed at these dif-  
 568 ferent mooring sites.

569 **4.3 Non-stationarity of internal tides on the NWS**

570 **4.3.1 Mean amplitude variability**

571 Spatial variations in the mean  $M_2$   $SSH_{BC}$  amplitude revealed several hot spot re-  
 572 gions, including around the major Indonesian Straits (Lombok, Ombai, Timor), on the  
 573 NWS near Rowley Shoals, and the Browse Basin regions. Furthermore, the model re-  
 574 vealed vast regions of standing wave-like characteristics throughout the domain, includ-

575 ing on the shelf between the 200 and 500 m isobaths (Fig 7a). The standing wave pat-  
 576 terns led to nodes and anti-nodes in  $SSH_{BC}$  that varied over spatial scales of roughly  
 577 one internal tide wave length (roughly 50 km on the shelf and 100 km in the deep basin).

578 Qualitatively, this agreed with the spatial variations from the altimetry-derived HRET  
 579 model (Fig 1). Some obvious differences between the HRET and the SUNTANS-derived  
 580 harmonic amplitudes were close to islands (e.g. Lombok Strait) and on the NWS in depths  
 581 less than 500 m. A known limitation of the satellite-filtering process is the necessity to  
 582 filter out signals in shallow water where the internal tides and barotropic tides vary over  
 583 similar length scales (e.g. Zaron 2019). The  $K_1$  component, which was dominant in the  
 584 Timor Sea but weak on the North West Shelf, also formed standing internal tide pat-  
 585 terns (Fig. 7b). It was also significantly larger than the  $K_1$  amplitude from the HRET  
 586 (not shown).

#### 587 **4.3.2 Regional variability of non-stationary metrics**

588 The non-stationary model was a far more suitable descriptor of the  $SSH_{BC}$  from  
 589 the 12-month model simulation in terms of the difference between TVFH and SVFH (Fig  
 590 8). On the shelf/ slope region (200 - 500 m), where all of the mooring sites examined here  
 591 were located, the TVFH parameter exceeded 50 % and was always greater than SVFH  
 592 (Table 7). In large parts of the Timor Sea and Browse Basin regions the TVFH exceeded  
 593 90 % (Fig 8a). Of note, is that TVFH was consistently lower in nodal regions (described  
 594 below) such as the KIM400 mooring site. This site had lower overall signal variance and  
 595 this analysis reveals that the signal is comprised of greater variability at other frequen-  
 596 cies or undergoes more severe amplitude modulation. PIL200 also appeared to straddle  
 597 a standing internal wave node point.

598 The variance fraction of the harmonic signals in the  $M_2$  and  $K_1$  bands ( $VF_m$ ) closely  
 599 resembled the mean harmonic amplitude with  $M_2$  dominance (60 - 90 % of variance) on  
 600 the NWS and throughout the Indo-Australian basin (Fig 9a). Conversely, the  $VF_{K_1}$  was  
 601 dominant in the Timor Sea. There were, however, isolated patches where this general  
 602 picture was violated. A notable example was the prevalence of the  $K_1$  band around PIL200  
 603 where  $VF_{K_1}$  was roughly 50 % ( $VF_{M_2}$  and  $VF_{K_1}$  were 43 and 23 %, respectively Ta-  
 604 ble 7). Likewise, there were regions of the Timor Sea, away from ITFTIS, where  $VF_{M_2} >$   
 605 50 %, whereas  $VF_{M_2}$  was only 2 % at ITFTIS. These isolated patches emphasise why

606 individual moorings may not be representative of the wider regional variability of inter-  
 607 nal tide-induced sea level fluctuations.

608 The non-stationary variance fraction ( $NSVF_m$ ) generally peaked in standing wave  
 609 node regions for both the  $M_2$  and  $K_1$  bands (Fig. 10). There were only large spatial re-  
 610 gions of non-stationary variance on the shelf in water depths less than 200 m where sea-  
 611 sonal variations in mixed layer depth led to no stratification, and no internal waves, and  
 612 a mean amplitude close to zero (see Fig. 7). The less predictable mooring sites (in terms  
 613 of the non-stationary model skill score in Table 6) also exhibited greater  $NSVF_{M_2}$  e.g.,  
 614 it was 59 % at PIL200 and 40 % at KIM400 (Table 7).

### 615 **4.3.3 Temporal evolution of standing internal tides**

616 The ITFTIS mooring was situated in the center of an anti-node, explaining the strong  
 617  $K_1$  signal at the site. Seasonal variations in  $|\eta_{K_1}|$  at the site, however, did not appear  
 618 to be due to spatial shifting of these standing wave regions but rather due to changes  
 619 in total amplitude (Fig 11). During October, when the mixed layer was relatively deep  
 620 in the Timor Sea,  $|\eta_{K_1}|$  was at a minimum, whereas during January, when there was near-  
 621 surface stratification, the amplitude peaked.

622 The node/anti-node variation is the main reason why the KIM200 and KIM400 have  
 623 such a different internal tide variability despite being relatively close in space. The KIM400  
 624 mooring was located in an  $M_2$  node region throughout the year (Fig 12), whereas the  
 625 KIM200 was in a node for part of the year (e.g. October), but in an anti-node during  
 626 January. Note that the baroclinic velocity will have the opposite response to  $SSH_{BC}$   
 627 and isotherm displacement amplitude; velocity will peak in the  $SSH_{BC}$  nodes and be  
 628 smallest in the anti-nodes see e.g. M. Rayson et al. (2012),.

### 629 **4.3.4 Summary of model results**

630 The key results from the 12-month ocean model non-stationary harmonic fit were:

- 631 • Internal tide amplitudes in all frequency bands exhibited standing wave patterns;
- 632 • Predictability at a given observation point generally coincided with the location  
 633 of nodes and anti-nodes and also with the total signal variance fraction in the sea-  
 634 sonal harmonics;

- 635 • The ability of both the non-stationary and stationary empirical harmonic mod-  
636 els to capture the total  $SSH_{BC}$  signal variance was regionally-dependent, with the  
637 Timor Sea being the most predictable and the Pilbara region (southern NWS) be-  
638 ing the least predictable.
- 639 • Overall, the non-stationary model captured more of the signal variance, as it in-  
640 cludes 7 times more frequencies and hence amplitude parameters than the station-  
641 ary model.
- 642 • In regions where the harmonic fit described zero percent of the variance, like on  
643 the shelf in water shallower than 200 m, a non-stationary fit is essential.

## 644 5 Discussion

645 Non-stationary internal tides are primarily believed to be caused by perturbations  
646 in the internal wave phase speed due to time-variable stratification, mean flow and rel-  
647 ative vorticity (Zaron & Egbert, 2014). In a two-dimensional wave field, phase speed per-  
648 turbations will cause shifts in the location of constructive and destructive interference,  
649 thus driving variability over length scales of less than one wave length (50 - 150 km). The  
650 dominant mesoscale flow feature in the NE Indian Ocean is the strong Indonesian Through-  
651 flow (ITF) that persistently flows in a westerly direction from roughly June to Decem-  
652 ber (Meyers et al., 1995). This flow breaks down into a series of eddies (instabilities) be-  
653 tween December and March when the northern Australian monsoon winds shift from south  
654 easterly to northwesterly (Feng & Wijffels, 2002). Monthly-averaged steric height  $SSH$   
655 and surface currents from the internal-tide resolving SUNTANS model exhibited these  
656 features. In particular, a N-S  $SSH$  gradient and strong westward surface flow around  
657 October 2013 (Fig. 13a). Whereas by January 2013, the mean N-S  $SSH$  gradient had  
658 relaxed and was replaced by a series of geostrophically-balanced mesoscale eddies (Fig.  
659 13b). The mode-1 linear phase speed, (Zhao et al., 2016)

$$c_1 = \frac{\omega}{(\omega^2 - f^2)^{1/2}} c$$

660 where  $f$  is the Coriolis frequency and  $c$  is given by Eq. 11, was calculated using changes  
661 in background stratification only. The phase speed was up to  $0.3 \text{ m s}^{-1}$  faster in the *aus-*  
662 *tral* summer compared with spring (February minus October) over the NWS and south  
663 of Indonesia (Fig. 13c). In the deeper regions of the Indo-Australian Basin, the phase  
664 speed difference was roughly  $0.1 \text{ m s}^{-1}$  slower, although this was in a region where the  
665 total phase speed was greater than  $3.0 \text{ m s}^{-1}$ .

666 To identify the temporal modulation of the internal tide amplitude between Indone-  
 667 sia and the NWS due to refraction and/or Doppler-shifting, we interpolated  $|\eta_{M2}(t)|$  along  
 668 a line between Lombok Strait and the Rowley Shoals (transect line shown in Fig. 13c).  
 669 Seasonal variation in  $|\eta_{M2}(t)|$  was evident at each location along the transect; for exam-  
 670 ple, along 10.5 °S there were two major peaks in  $|\eta_{M2}(t)|$ , one in January and one in June  
 671 2014. Conversely, along 11 °S there was a single peak around February 2014. These dif-  
 672 ferences in seasonal peaks over such short distances can partly be explained by varia-  
 673 tions in arrival time due to changes in phase speed (Fig 14b). By assuming for simplic-  
 674 ity that wave propagation is one-dimensional, we calculated the propagation time,  $\tau(y, t)$ ,  
 675 from the time-varying phase speed along the transect line using

$$\tau(y, t) = \int_0^y \frac{1}{c_1(y', t)} dy',$$

676 where  $y$  is the distance along the transect line. Contours of  $\tau(y, t)$  help identify the drivers  
 677 of spatial differences in  $|\eta_{M2}(t)|$  due to stratification-induced refraction (black contours  
 678 on Fig. 14). The peak in  $|\eta_{M2}(t)|$  at 11 °S during March 2014 corresponded with a pe-  
 679 riod when the line of constant propagation time migrated further south due to the in-  
 680 creased phase speed south of Lombok Strait. Lines of constant propagation time were  
 681 less indicative of amplitude modulations further from the primary internal tide source  
 682 regions, e.g., between 12 and 16 °S in Fig. 14a. This discrepancy is likely due to other  
 683 processes causing perturbations in the mode-1 phase speed (namely the mean flow and  
 684 vorticity), and also due to the wave propagation being two-dimensional.

685 Doppler-shifting of the internal tide harmonics may be inferred using the present  
 686 analysis by finding time periods when the signal amplitude was reduced. To calculate  
 687 two-dimensional variations in amplitude reduction, we performed a directional decom-  
 688 position of the complex harmonic amplitudes using the technique outlined in Gong et  
 689 al. (2020). This technique takes a 2D Fourier transform of the complex spatial internal  
 690 tide amplitude, filters the horizontal wavenumbers (that are both positive and negative)  
 691 according to a directional band of choice, and then takes the inverse Fourier transform.  
 692 The SE propagating component (filter band of 0 to 90 degrees CCW from E) isolated  
 693 the internal tide originating from Indonesia, while the NW propagating component iso-  
 694 lated the NWS-generated internal tide (Fig 15). Temporal modulations of the SE com-  
 695 ponent were most pronounced in the centre of the Indo-Australian basin and on the NWS  
 696 slope. The modulating component on the NWS was evident in the multi-directional sig-  
 697 nal (e.g. Fig 10), and is described in detail in (M. Rayson et al., 2012). Between 8 and

698 14 ° S, the SE propagating component, which originated near Lombok strait, was 1 - 2  
 699 cm (50 % or more) smaller during October than it was during February (Fig 15d-f). Like-  
 700 wise, the NW propagating component, which originated along the NWS, was 1 - 2 cm  
 701 smaller near Indonesia during October than it was in February (Fig 15a-c). We attribute  
 702 the amplitude reduction in  $SSH_{BC}$  around October to Doppler shifting of the low-mode  
 703 internal tide caused by the strong ITF flow during this period (e.g. Fig. 13a). Energy  
 704 fluxes from internal waves into the background mean flow are also likely to cause some  
 705 of the amplitude variations (e.g., Dunphy & Lamb, 2014).

706 A conventional view of internal tides at a fixed site, like a mooring, is that the lo-  
 707 cal barotropic forcing frequency will directly transfer into the frequency content of the  
 708 internal motions. Multiple generation sites and long propagation distances, however, lead  
 709 to high spatial variability of internal wave-induced ocean scalars (i.e., decorrelation length  
 710 scales of less than one internal tide wave length). For example, despite the  $M_2$  barotropic  
 711 tide being dominant on the NWS (P. E. Holloway, 1983), the KIM200 mooring was the  
 712 only site where the  $M_2$  baroclinic component was dominant throughout the year (see Fig.  
 713 6). This is contrary to the conventional view that the  $M_2$  internal tide is dominant (e.g.,  
 714 P. Holloway, 2001; M. Rayson et al., 2012; Kelly et al., 2014). While this conventional  
 715 picture was generally true in the numerical model solution (see e.g., Fig. 7), the results  
 716 presented here indicate that large spatial variations in amplitude occur over short dis-  
 717 tances of generally less than one wave length. Conversely in the Timor Sea, there is a  
 718  $M_2$  tidal amphidrome resulting in the dominance of diurnal barotropic tides (see e.g.,  
 719 Robertson and Field (2008)). Based on an analysis of the ITFTIS mooring it may be  
 720 tempting to conclude that the  $K_1$  internal tide is therefore also dominant in the Timor  
 721 Sea. The regional internal tide model highlighted, however, that there are regions within  
 722 30 km of the mooring where the  $M_2$  component is dominant (Fig. 9a), likely due to re-  
 723 motely generated internal tides. The high spatial variability is an important consider-  
 724 ation to take into account when choosing mooring field sampling strategies to study the  
 725 internal tide (or in trying to interpret data from a mooring). Finally, we have not pre-  
 726 sented any analysis of internal tide-induced velocity perturbations. It should be noted  
 727 that in places where standing internal waves are dominant (almost everywhere in this  
 728 domain), regions of small  $SSH_{BC}$  or isotherm displacement amplitude variance will likely  
 729 have large baroclinic velocity variance. Interpretation of individual and isolated in situ

730 observations requires knowledge of the broader spatial context, namely the regional in-  
 731 ternal tide interference patterns.

## 732 **6 Conclusions**

733 A key output of harmonically-decomposing internal tide amplitude or  $SSH_{BC}$  from  
 734 primitive equation ocean model solutions, like our one-year SUNTANS solution for the  
 735 Indo-Australian Basin, is an internal tide climatological database. By including the “sea-  
 736 sonal sidelines” in our harmonic analysis, as hinted at in Arbic et al. (2015), we have shown  
 737 that a greater amount of internal tide variance is captured, particularly around shelf re-  
 738 gions (see e.g., Fig. 8, Tab. 4). This climatology has practical applications including:  
 739 allowing the removal of internal tide signals for future satellite altimetry missions (e.g.,  
 740 Morrow et al., 2019); or in supplying boundary conditions for regional internal wave mod-  
 741 elling applications (e.g., Gong et al., 2020). Here we have constructed a regional inter-  
 742 nal tide database and a global database that could readily be calculated using output  
 743 from a global internal-tide resolving model, e.g., the  $1/25^\circ$  HyCOM model in Savage et  
 744 al. (2017) or the  $1/48^\circ$  LLC4320 MITGCM run in Torres et al. (2018).

745 Various studies, including this one, have demonstrated that tidal harmonics are a  
 746 useful description of internal tide variability when applied over short time periods (gen-  
 747 erally less than a month). The most important aspect of internal tide prediction is how  
 748 to model the temporal modulation of these short time window amplitudes. Here, we used  
 749 a seasonal harmonic model that was motivated by the modulation of the Timor Sea in-  
 750 ternal tides, which are primarily driven by seasonal changes in the ocean stratification  
 751 (Kelly et al., 2014). This seasonal model is less suited to other regions of the globe (the  
 752 PIL200 site is one example) where internal tide variations are due to more transient (ape-  
 753 riodic) features like mesoscale eddies. To model the temporal modulation in these re-  
 754 gions, non-parametric techniques, like splines or Gaussian processes, are likely to be bet-  
 755 ter suited. These methods, however, rely on having recent data to make predictions of  
 756 internal tides into the short future i.e. so-called data-driven statistical techniques. In re-  
 757 gions where internal tide prediction is important for operational decision making, these  
 758 data-driven techniques will be necessary. Our parametric seasonal harmonics provided  
 759 a better prediction of the internal tides throughout most of the study region and there-  
 760 fore are a useful starting point for these more data-intensive statistical modelling tech-  
 761 niques.

## 762 Acknowledgments

763 This work was supported by the Australian Research Council Industrial Transformation  
 764 Research Hub for Offshore Floating Facilities (IH140100012). This work was supported  
 765 by resources provided by the Pawsey Supercomputing Centre with funding from the Aus-  
 766 tralian Government and the Government of Western Australia. Observation data was  
 767 sourced from Australia’s Integrated Marine Observing System (IMOS) — IMOS is en-  
 768 abled by the National Collaborative Research Infrastructure strategy (NCRIS). Qual-  
 769 ity controlled observation data is available on the Australian Ocean Data Network (<https://portal.aodn.org.au>).  
 770 Numerical model tide data is available at: [tpxo.net/regional](http://tpxo.net/regional). Initial and boundary con-  
 771 dition data are at ([https://resources.marine.copernicus.eu/documents/PUM/CMEMS-](https://resources.marine.copernicus.eu/documents/PUM/CMEMS-GLO-PUM-001-030.pdf)  
 772 [GLO-PUM-001-030.pdf](https://resources.marine.copernicus.eu/documents/PUM/CMEMS-GLO-PUM-001-030.pdf)). Processed numerical model output and observation data are  
 773 archived on the UWA library research repository (<https://doi.org/10.26182/8jx9-m532>).

## 774 References

- 775 Arbic, B. K., Lyard, F., Ponte, A., Ray, R. D., Richman, J. G., Shriver, J. F., . . .  
 776 Zhao, Z. (2015). Tides and the SWOT mission: Transition from Science  
 777 Definition Team to Science Team. (January), 1–8.
- 778 Buijsman, M. C., Arbic, B. K., Richman, J. G., Shriver, J. F., Wallcraft, A. J., &  
 779 Zamudio, L. (2017, 7). Semidiurnal internal tide incoherence in the equa-  
 780 torial Pacific. *Journal of Geophysical Research: Oceans*, *122*(7), 5286–5305.  
 781 Retrieved from [https://onlinelibrary.wiley.com/doi/abs/10.1002/](https://onlinelibrary.wiley.com/doi/abs/10.1002/2016JC012590)  
 782 [2016JC012590](https://onlinelibrary.wiley.com/doi/abs/10.1002/2016JC012590) doi: 10.1002/2016JC012590
- 783 Castaño-Tierno, A., Mohino, E., Rodríguez-Fonseca, B., & Losada, T. (2018). Re-  
 784 visiting the CMIP5 Thermocline in the Equatorial Pacific and Atlantic Oceans.  
 785 *Geophysical Research Letters*, *45*(23), 963–12. doi: 10.1029/2018GL079847
- 786 Colosi, J. A., & Munk, W. (2006). Tales of the venerable Honolulu tide gauge. *Jour-*  
 787 *nal of Physical Oceanography*, *36*(6), 967–996. doi: 10.1175/JPO2876.1
- 788 Dee, D. P., Uppala, S. M., Simmons, A. J., Berrisford, P., Poli, P., Kobayashi, S., . . .  
 789 Vitart, F. (2011). The ERA-Interim reanalysis: Configuration and performance  
 790 of the data assimilation system. *Quarterly Journal of the Royal Meteorological*  
 791 *Society*, *137*(656), 553–597. doi: 10.1002/qj.828
- 792 Ducet, N., Le Traon, P. Y., & Reverdin, G. (2000). Global high-resolution  
 793 mapping of ocean circulation from TOPEX/Poseidon and ERS-1 and -

- 794 2. *Journal of Geophysical Research: Oceans*, 105(C8), 19477–19498. doi:  
795 10.1029/2000jc900063
- 796 Dunphy, M., & Lamb, K. G. (2014). Focusing and vertical mode scattering of the  
797 first mode internal tide by mesoscale eddy interaction. *Journal of Geophysical*  
798 *Research: Oceans*, 119(1), 523–536. doi: 10.1002/2013JC009293
- 799 Egbert, G., & Erofeeva, S. (2002). Efficient inverse modeling of barotropic ocean  
800 tides. *Journal of Atmospheric & Oceanic Technology*, 183–204. Retrieved  
801 from <http://search.ebscohost.com/login.aspx?direct=true&profile=eohost&scope=site&authtype=crawler&jrnl=07390572&AN=5921008&h=7UU9nfX1%2BWu2UVAMNCDBGMUyLT10aMoBFENs0sL0wG%2FxonLEHdBqyaMiw4E2%2BgjPDBSm2lrWDilU6meYSmzttA%3D%3D&crl=c>  
802  
803  
804
- 805 Egbert, G. D., & Ray, R. D. (2017). Tidal prediction. *Journal of Marine Research*,  
806 75(3), 189–237. doi: 10.1357/002224017821836761
- 807 Fairall, C. W., Bradley, E. F., Hare, J. E., Grachev, A. A., & Edson, J. B.  
808 (2003). Bulk parameterization of air-sea fluxes: Updates and verification  
809 for the COARE algorithm. *Journal of Climate*, 16(4), 571–591. doi:  
810 10.1175/1520-0442(2003)016<0571:BPOASF>2.0.CO;2
- 811 Feng, M., & Wijffels, S. (2002). Intraseasonal variability in the SEC of the East In-  
812 dian ocean. *J. Phys. Oceanogr.*, 32, 265–277.
- 813 Foreman, M. G. G. (1977). *Manual for tidal heights analysis and prediction* (Tech.  
814 Rep.). Institute of Ocean Sciences, Patricia Bay.
- 815 Fringer, O. B., Gerritsen, M., & Street, R. L. (2006). An unstructured-grid, finite-  
816 volume, nonhydrostatic, parallel coastal ocean simulator. *Ocean Modelling*,  
817 14(3-4), 139–173. doi: 10.1016/j.ocemod.2006.03.006
- 818 Gong, Y., Rayson, M. D., Jones, N. L., & Iver, G. N. (2020). Directional decompo-  
819 sition of internal tides propagating from multiple generation sites. *under review*  
820 *in Ocean Modelling*.
- 821 Gong, Y., Rayson, M. D., Jones, N. L., & Ivey, G. N. (2019). The Effects of Re-  
822 mote Internal Tides on Continental Slope Internal Tide Generation. *Journal of*  
823 *Physical Oceanography*, 49(6), 1651–1668. doi: 10.1175/jpo-d-18-0180.1
- 824 Grimshaw, R., Pelinovsky, E., Stepanyants, Y., & Talipova, T. (2006). Modelling  
825 internal solitary waves on the Australian North West Shelf. *Marine and Fresh-*  
826 *water Research*, 57(3), 265. doi: 10.1071/mf05016

- 827 Holloway, P. (2001). A regional model of the semidiurnal internal tide on the Aus-  
 828 tralian North West Shelf. *Journal of Geophysical Research: Oceans* (1978  
 829 ..., 106. Retrieved from [http://onlinelibrary.wiley.com/doi/10.1029/  
 830 2000JC000675/full](http://onlinelibrary.wiley.com/doi/10.1029/2000JC000675/full)
- 831 Holloway, P., Pelinovsky, E., Talipova, T., & Barnes, B. (1997). A nonlinear model  
 832 of internal tide transformation on the Australian North West Shelf. *Journal of  
 833 Physical*, 27, 871–896. Retrieved from [http://journals.ametsoc.org/doi/  
 834 pdf/10.1175/1520-0485\(1997\)027%3C0871:ANMOIT%3E2.O.CO;2](http://journals.ametsoc.org/doi/pdf/10.1175/1520-0485(1997)027%3C0871:ANMOIT%3E2.O.CO;2)
- 835 Holloway, P. E. (1983). *Tides on the australian north-west shelf* (Vol. 34) (No. 1).  
 836 doi: 10.1071/MF9830213
- 837 Huess, V., & Andersen, O. B. (2001). Seasonal variation in the main tidal con-  
 838 stituent from Altimetry. *Geophysical Research Letters*, 28(4), 567–570. doi: 10  
 839 .1029/2000GL011921
- 840 Kelly, S. M., Jones, N. L., Ivey, G. N., & Lowe, R. J. (2014). Internal-Tide Spec-  
 841 troscopy and Prediction in the Timor Sea. *Journal of Physical Oceanography*,  
 842 45(1), 64–83. Retrieved from <http://dx.doi.org/10.1175/JPO-D-14-0007.1>  
 843 doi: 10.1175/JPO-D-14-0007.1
- 844 Kelly, S. M., & Nash, J. D. (2010, 12). Internal-tide generation and destruction by  
 845 shoaling internal tides. *Geophysical Research Letters*, 37(23), n/a-n/a. Re-  
 846 trieved from <http://doi.wiley.com/10.1029/2010GL045598> doi: 10.1029/  
 847 2010GL045598
- 848 Mellor, G., & Yamada, T. (1982). Development of a Turbulence Closure Model for  
 849 Geophysical Fluid Problems. *Reviews of Geophysics and Space Physics*, 20(4),  
 850 851–875.
- 851 Meyers, G., Bailey, R. J., & Worby, A. P. (1995). Geostrophic transport of Indone-  
 852 sian throughflow. *Deep-Sea Research Part I*, 42(7), 1163–1174. doi: 10.1016/  
 853 0967-0637(95)00037-7
- 854 Morrow, R., Fu, L. L., Arduin, F., Benkiran, M., Chapron, B., Cosme, E., ...  
 855 Zaron, E. (2019). Global observations of fine-scale ocean surface topography  
 856 with the Surface Water and Ocean Topography (SWOT) Mission. *Frontiers in  
 857 Marine Science*, 6(APR), 1–19. doi: 10.3389/fmars.2019.00232
- 858 Munk, W. H., & Cartwright, D. (1966). TIDAL SPECTROSCOPY AND PREDIC-  
 859 TION. *PHILOSOPHICAL TRANSACTIONS OF THE ROYAL SOCIETY*

- 860 *OF LONDON*, 259(1105), 533–581. doi: 10.2307/j.ctt211qv60.7
- 861 Murphy, A. (1988). Skill scores based on the mean square error and their relation-  
 862 ships to the correlation coefficient. *Monthly weather review*. Retrieved from  
 863 [http://journals.ametsoc.org/doi/abs/10.1175/1520-0493\(1988\)116%](http://journals.ametsoc.org/doi/abs/10.1175/1520-0493(1988)116%3C2417:SSBOTM%3E2.0.CO%3B2)  
 864 [3C2417:SSBOTM%3E2.0.CO%3B2](http://journals.ametsoc.org/doi/abs/10.1175/1520-0493(1988)116%3C2417:SSBOTM%3E2.0.CO%3B2)
- 865 Nash, J. D., Kelly, S. M., Shroyer, E. L., Moum, J. N., & Duda, T. F. (2012). The  
 866 unpredictable nature of internal tides on continental shelves. *Journal of Physi-*  
 867 *cal Oceanography*, 42(11), 1981–2000. doi: 10.1175/JPO-D-12-028.1
- 868 Nash, J. D., Shroyer, E., Kelly, S., Inall, M., Duda, T., Levine, M., . . . Musgrave,  
 869 R. (2012, 6). Are Any Coastal Internal Tides Predictable? *Oceanog-*  
 870 *raphy*, 25(2), 80–95. Retrieved from [http://dx.doi.org/10.5670/](http://dx.doi.org/10.5670/oceanog.2012.44)  
 871 [https://tos.org/oceanography/article/are-any](https://tos.org/oceanography/article/are-any-coastal-internal-tides-predictable)  
 872 [-coastal-internal-tides-predictable](https://tos.org/oceanography/article/are-any-coastal-internal-tides-predictable) doi: 10.5670/oceanog.2012.44
- 873 Nelson, A. D., Arbic, B. K., Zaron, E. D., Savage, A. C., Richman, J. G., Buijsman,  
 874 M. C., & Shriver, J. F. (2019). Toward Realistic Nonstationarity of Semid-  
 875 urnal Baroclinic Tides in a Hydrodynamic Model. *Journal of Geophysical*  
 876 *Research: Oceans*, 124(9), 6632–6642. doi: 10.1029/2018JC014737
- 877 Ponte, A. L., & Klein, P. (2015). Incoherent signature of internal tides on sea level  
 878 in idealized numerical simulations. *Geophysical Research Letters*, 42(5), 1520–  
 879 1526. doi: 10.1002/2014GL062583
- 880 Rainville, L., & Pinkel, R. (2006). Propagation of low-mode internal waves through  
 881 the ocean. *Journal of Physical Oceanography*, 36(6), 1220–1236. doi: 10.1175/  
 882 JPO2889.1
- 883 Ray, R. D., & Zaron, E. D. (2011). Non-stationary internal tides observed with  
 884 satellite altimetry. *Geophysical Research Letters*, 38(17), 1–5. doi: 10.1029/  
 885 2011GL048617
- 886 Rayson, M., Ivey, G., Jones, N., & Fringer, O. (2018). Resolving high-frequency  
 887 internal waves generated at an isolated coral atoll using an unstructured grid  
 888 ocean model. *Ocean Modelling*, 122. doi: 10.1016/j.ocemod.2017.12.007
- 889 Rayson, M., Jones, N., & Ivey, G. (2012). Temporal variability of the standing in-  
 890 ternal tide in the Browse Basin, Western Australia. *Journal of Geophysical Re-*  
 891 *search: Oceans*, 117(6). doi: 10.1029/2011JC007523
- 892 Rayson, M. D., Gross, E. S., & Fringer, O. B. (2015, 5). Modeling the tidal and sub-

- 893 tidal hydrodynamics in a shallow, micro-tidal estuary. *Ocean Modelling*, 89,  
894 29–44. Retrieved from [https://linkinghub.elsevier.com/retrieve/pii/](https://linkinghub.elsevier.com/retrieve/pii/S1463500315000207)  
895 S1463500315000207 doi: 10.1016/j.ocemod.2015.02.002
- 896 Rayson, M. D., Ivey, G. N., Jones, N. L., & Fringer, O. B. (2017). Scott Reef SUN-  
897 TANS Hydrodynamic Modelling Study. , 1–208.
- 898 Rayson, M. D., Jones, N. L., & Ivey, G. N. (2019). Observations of Large-Amplitude  
899 Mode-2 Nonlinear Internal Waves on the Australian North West Shelf. *Journal*  
900 *of Physical Oceanography*, 49(1), 309–328. doi: 10.1175/jpo-d-18-0097.1
- 901 Robertson, R., & Field, A. (2008). Baroclinic tides in the Indonesian seas: Tidal  
902 fields and comparisons to observations. *Journal of Geophysical Research:*  
903 *Oceans*, 113(7), 1–22. doi: 10.1029/2007JC004677
- 904 Savage, A. C., Arbic, B. K., Richman, J. G., Shriver, J. F., Alford, M. H., Buijs-  
905 man, M. C., ... Zamudio, L. (2017, 3). Frequency content of sea surface  
906 height variability from internal gravity waves to mesoscale eddies. *Journal of*  
907 *Geophysical Research: Oceans*, 122(3), 2519–2538. Retrieved from [http://](http://doi.wiley.com/10.1002/2016JC012331)  
908 [doi.wiley.com/10.1002/2016JC012331](http://doi.wiley.com/10.1002/2016JC012331) doi: 10.1002/2016JC012331
- 909 Shriver, J. F., Richman, J. G., & Arbic, B. K. (2014, 5). How stationary are the  
910 internal tides in a high-resolution global ocean circulation model? *Journal of*  
911 *Geophysical Research: Oceans*, 119(5), 2769–2787. Retrieved from [http://doi](http://doi.wiley.com/10.1002/2013JC009423)  
912 [.wiley.com/10.1002/2013JC009423](http://doi.wiley.com/10.1002/2013JC009423) doi: 10.1002/2013JC009423
- 913 Stammer, D., Ray, R. D., Andersen, O. B., Arbic, B. K., Bosch, W., Carrère, L.,  
914 ... Yi, Y. (2014, 9). Accuracy assessment of global barotropic ocean tide  
915 models. *Reviews of Geophysics*, 52(3), 243–282. Retrieved from [http://](http://doi.wiley.com/10.1002/2014RG000450)  
916 [doi.wiley.com/10.1002/2014RG000450](http://doi.wiley.com/10.1002/2014RG000450) doi: 10.1002/2014RG000450
- 917 Torres, H. S., Klein, P., Menemenlis, D., Qiu, B., Su, Z., Wang, J., ... Fu, L. L.  
918 (2018). Partitioning Ocean Motions Into Balanced Motions and Internal  
919 Gravity Waves: A Modeling Study in Anticipation of Future Space Mis-  
920 sions. *Journal of Geophysical Research: Oceans*, 123(11), 8084–8105. doi:  
921 10.1029/2018JC014438
- 922 Zaron, E. D. (2019). Baroclinic tidal sea level from exact-repeat mission altime-  
923 try. *Journal of Physical Oceanography*, 49(1), 193–210. doi: 10.1175/JPO-D-18-  
924 -0127.1
- 925 Zaron, E. D., & Egbert, G. D. (2014). Time-Variable Refraction of the Internal

- 926 Tide at the Hawaiian Ridge. *Journal of Physical Oceanography*, 44(2), 538–  
927 557. Retrieved from [http://journals.ametsoc.org/doi/abs/10.1175/  
928 JPO-D-12-0238.1](http://journals.ametsoc.org/doi/abs/10.1175/JPO-D-12-0238.1) doi: 10.1175/JPO-D-12-0238.1
- 929 Zhao, Z., Alford, M. H., Girton, J. B., Rainville, L., & Simmons, H. L. (2016).  
930 Global Observations of Open-Ocean Mode-1 M <sub>2</sub> Internal Tides.  
931 *Journal of Physical Oceanography*, 46(6), 1657–1684. Retrieved from  
932 <http://journals.ametsoc.org/doi/10.1175/JPO-D-15-0105.1> doi:  
933 10.1175/JPO-D-15-0105.1

## FIGURES

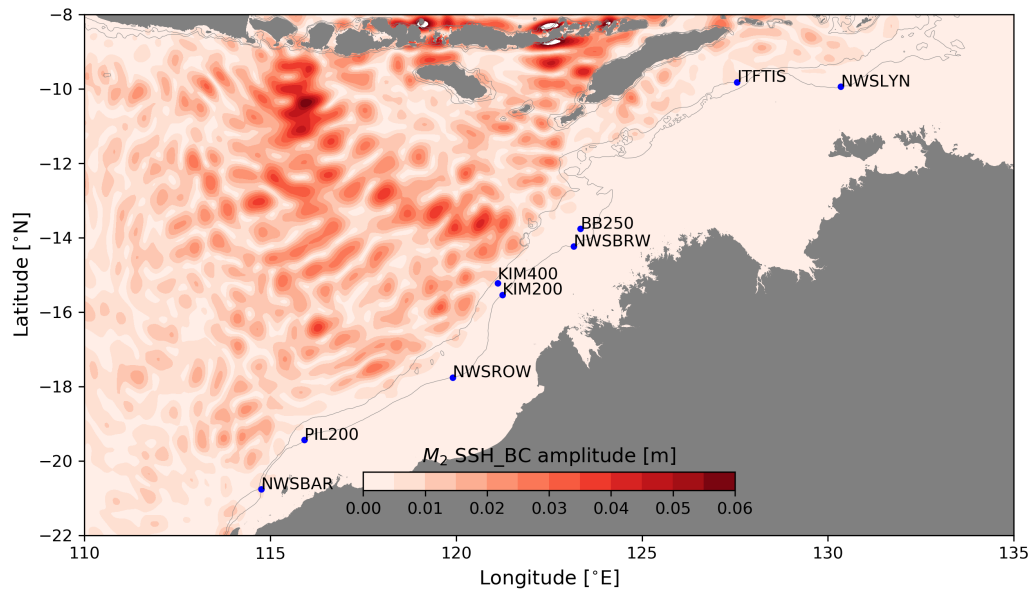


**Figure 1.** Map of the field sites with the  $M_2$  baroclinic sea surface height amplitude [m] from Zaron (2019) overlaid. Grey lines indicate the 200 and 500 m depth contours that highlight the edge of the continental shelf.

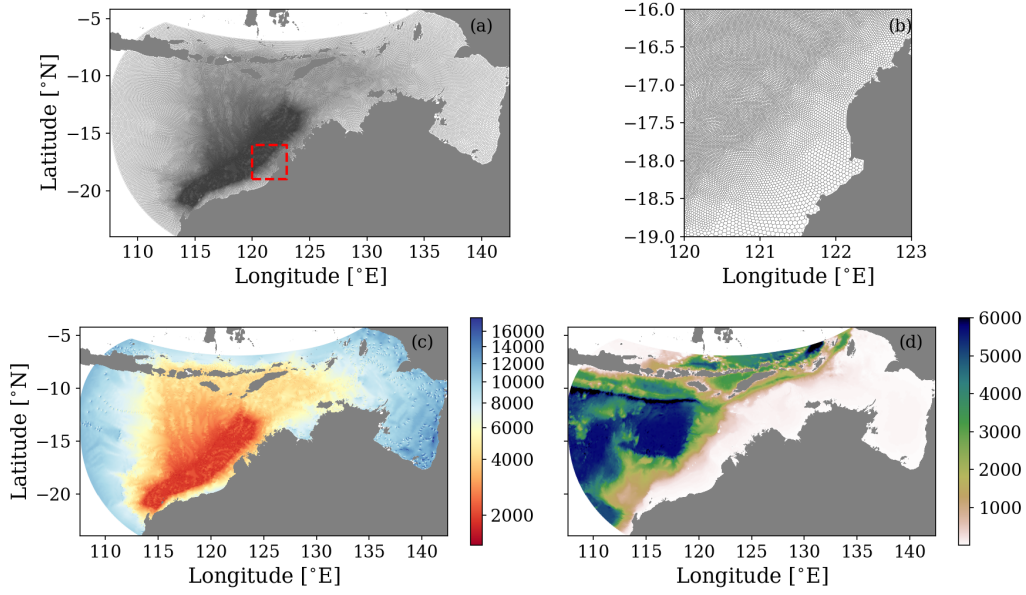


**Figure 2.** (a,b) Unstructured hexagonal-dominant SUNTANS mesh encompassing the Indo-Australian Basin, North West Shelf, Timor Sea and Gulf of Carpentaria. (c) Horizontal grid resolution [m] noting that colours are on a nonlinear scale and (d) model bathymetry [m].

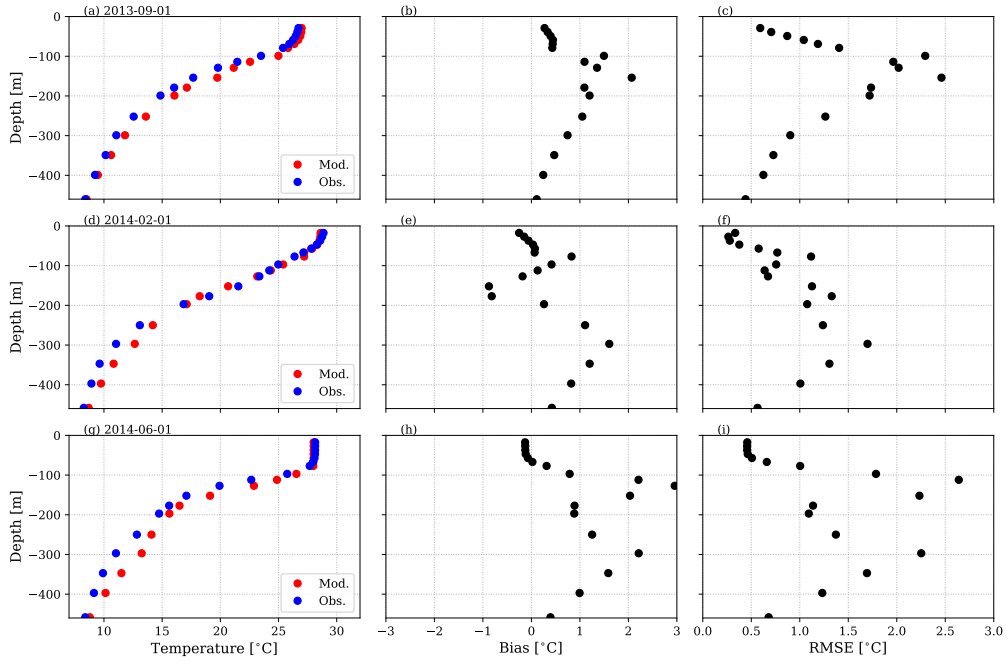


**Figure 3.** Quantitative SUNTANS model evaluation metrics against in situ temperature observations from the ITFTIS mooring of (left column) monthly-averaged temperature, (middle column) temperature bias, and (right column) temperature root mean square error. Each row corresponds with monthly-averages for September 2013, February 2014 and June 2014.

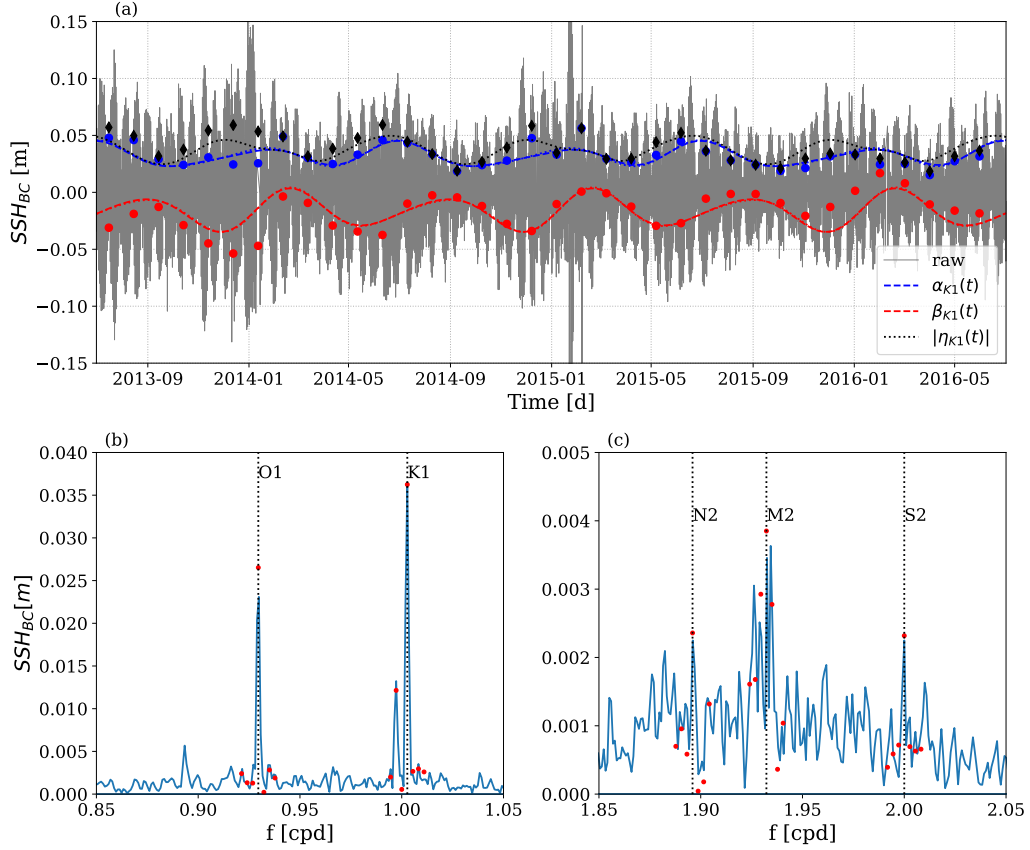


**Figure 4.** (a) 3-year time series of baroclinic sea surface height [m] at the Timor Sea (ITFTIS) mooring. Blue and red dots indicate the real and imaginary  $K_1$  amplitudes, respectively, from harmonic fitting 30 d segments, while the black dots indicate the complex amplitude magnitude. The dashed lines indicate the seasonal harmonic model fit to the discrete amplitudes. (b) and (c) are the discrete Fourier transform amplitude for the diurnal and semidiurnal bands, respectively (note the change in vertical scale). Red dots in (b) and (c) indicate the least-squares fit amplitude of the tidal bands plus the annual harmonics. Note the different vertical scales in (b) and (c)

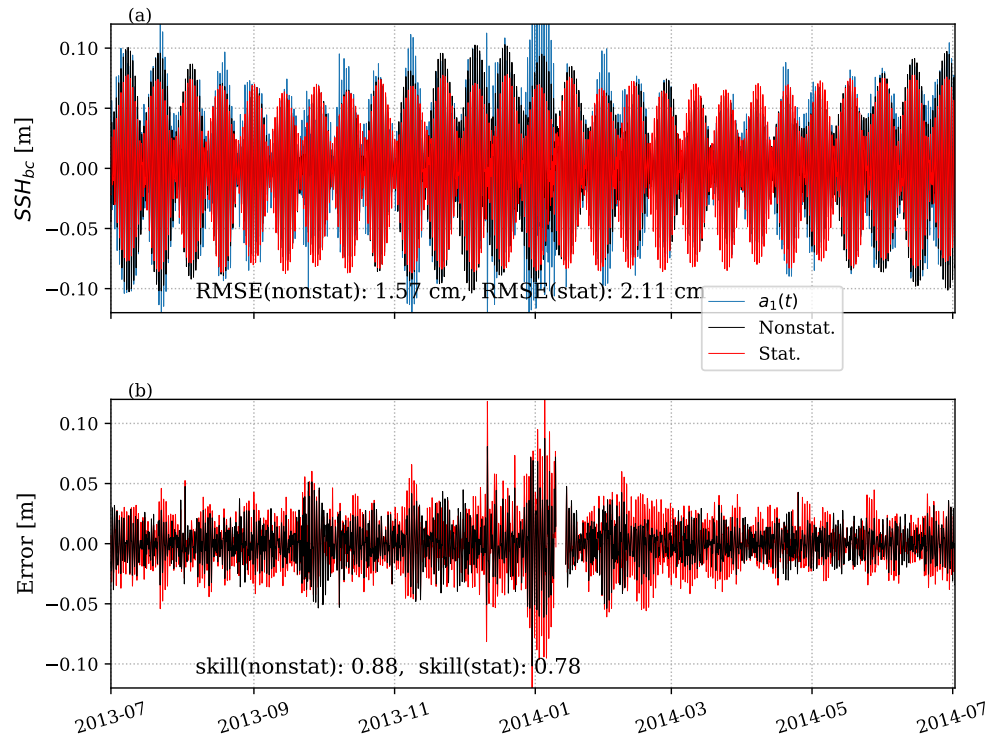


**Figure 5.** (Top) Baroclinic sea surface height perturbation ( $SSH_{BC}$ ) at the ITFTIS mooring with the nonstationary (black) and stationary models (overlaid). (Bottom) Error (model-observed) for the nonstationary (black) and stationary (red) models.

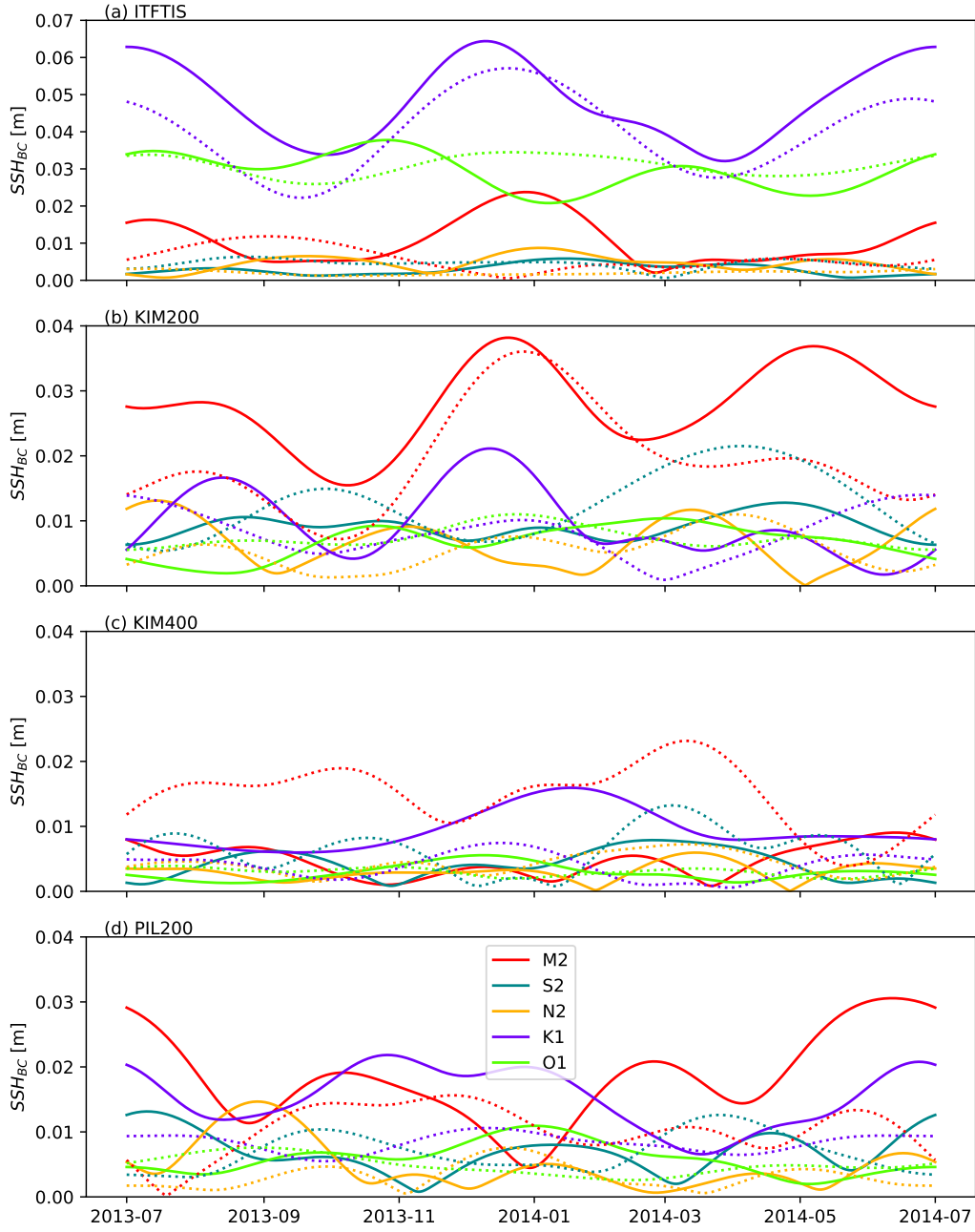


**Figure 6.** Seasonal modulation of  $|\eta_m(t)|$  (Eq. 5) for each of the five primary tidal harmonics at (a) ITFTIS, (b) KIM200, (c) KIM400, and (d) PIL200 mooring locations. The solid lines in each panel indicate fits to the *in situ* data and dotted lines are the SUNTANS model data. Note the different vertical scale in (a).

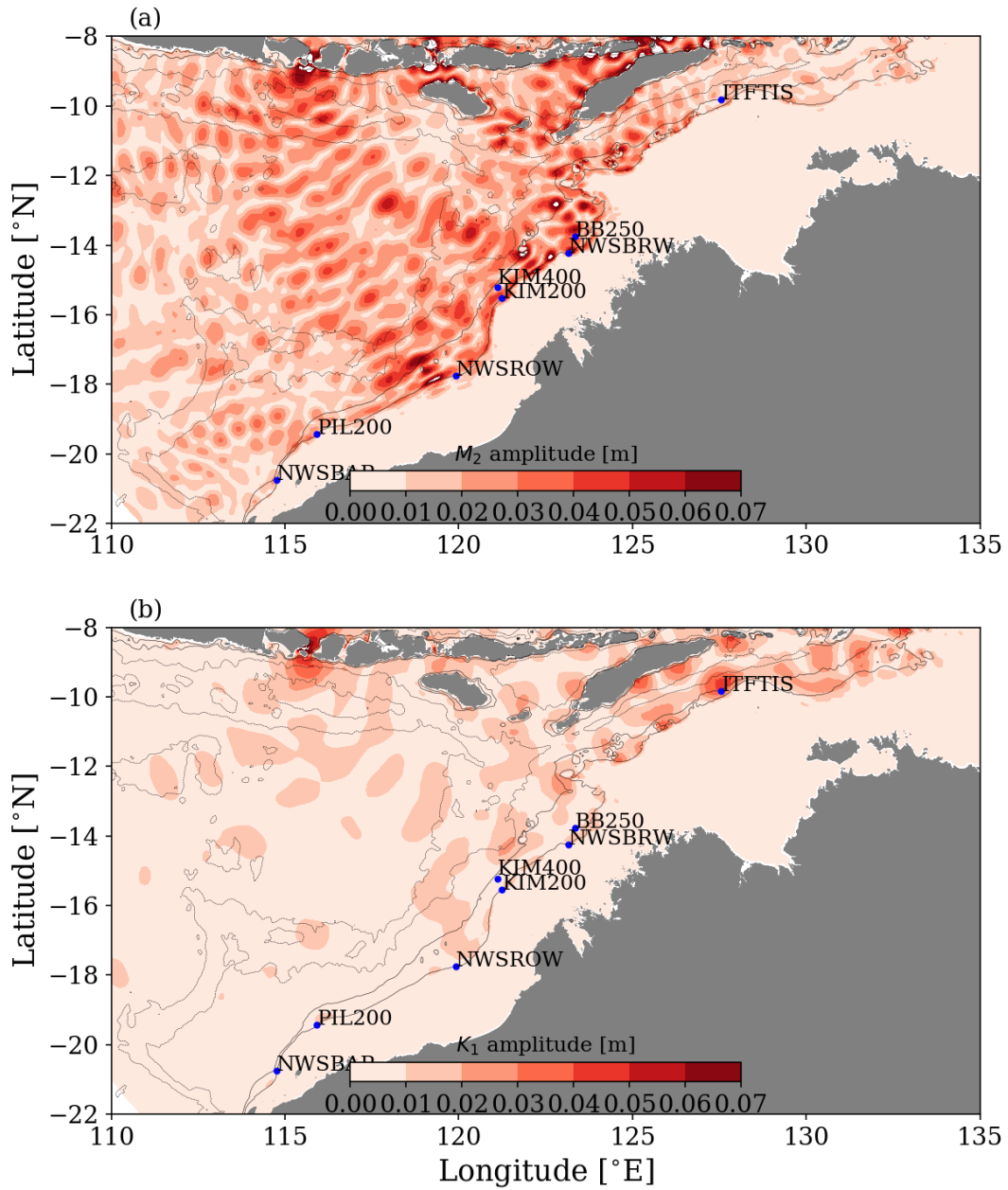


**Figure 7.** Mean baroclinic sea surface height harmonic amplitudes for (a) the  $M_2$  and (b) the  $K_1$  tidal constituents from the 12-month SUNTANS simulation.

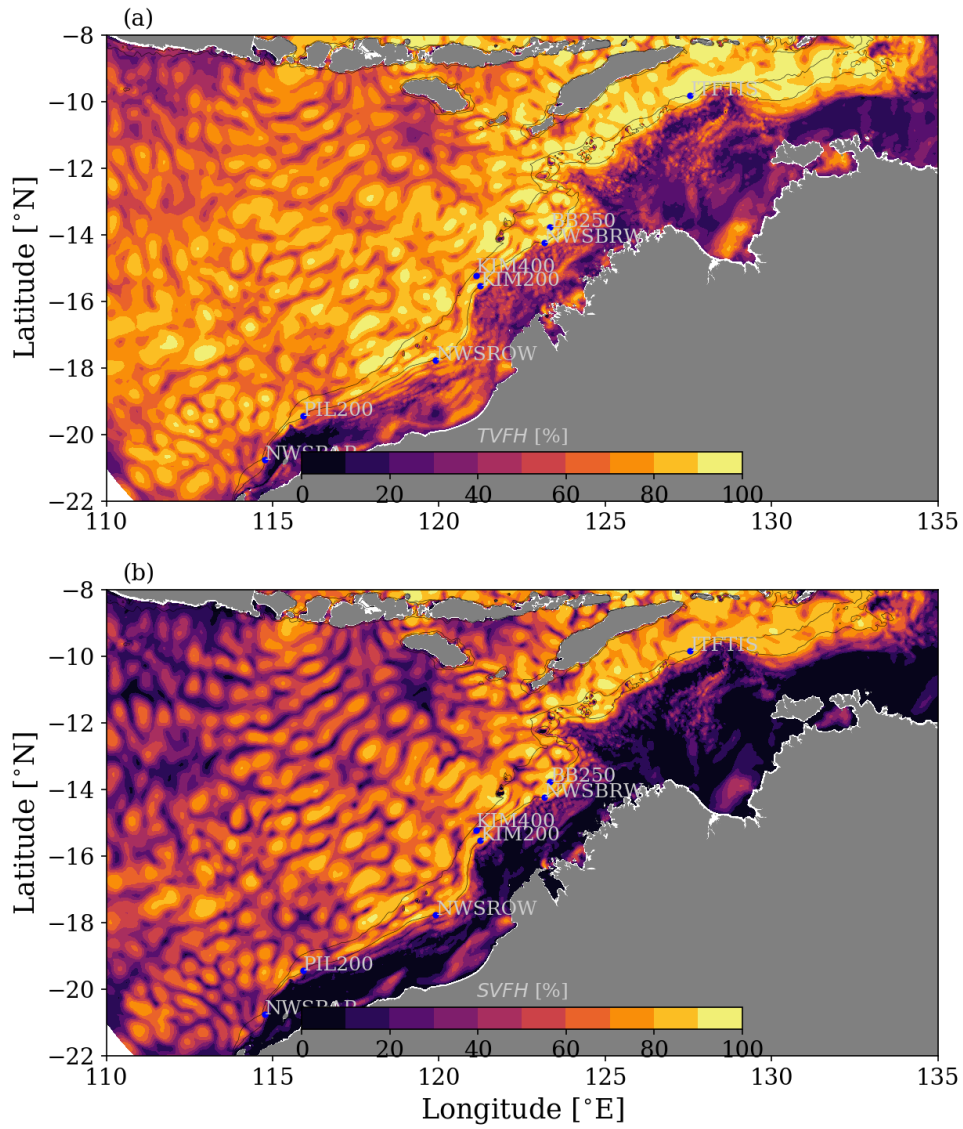


**Figure 8.** Percentage of variance of the SUTANS baroclinic SSH (Eq. 8) explained by the (a) non-stationary (TVFH) and (b) stationary harmonic models (SVFH).

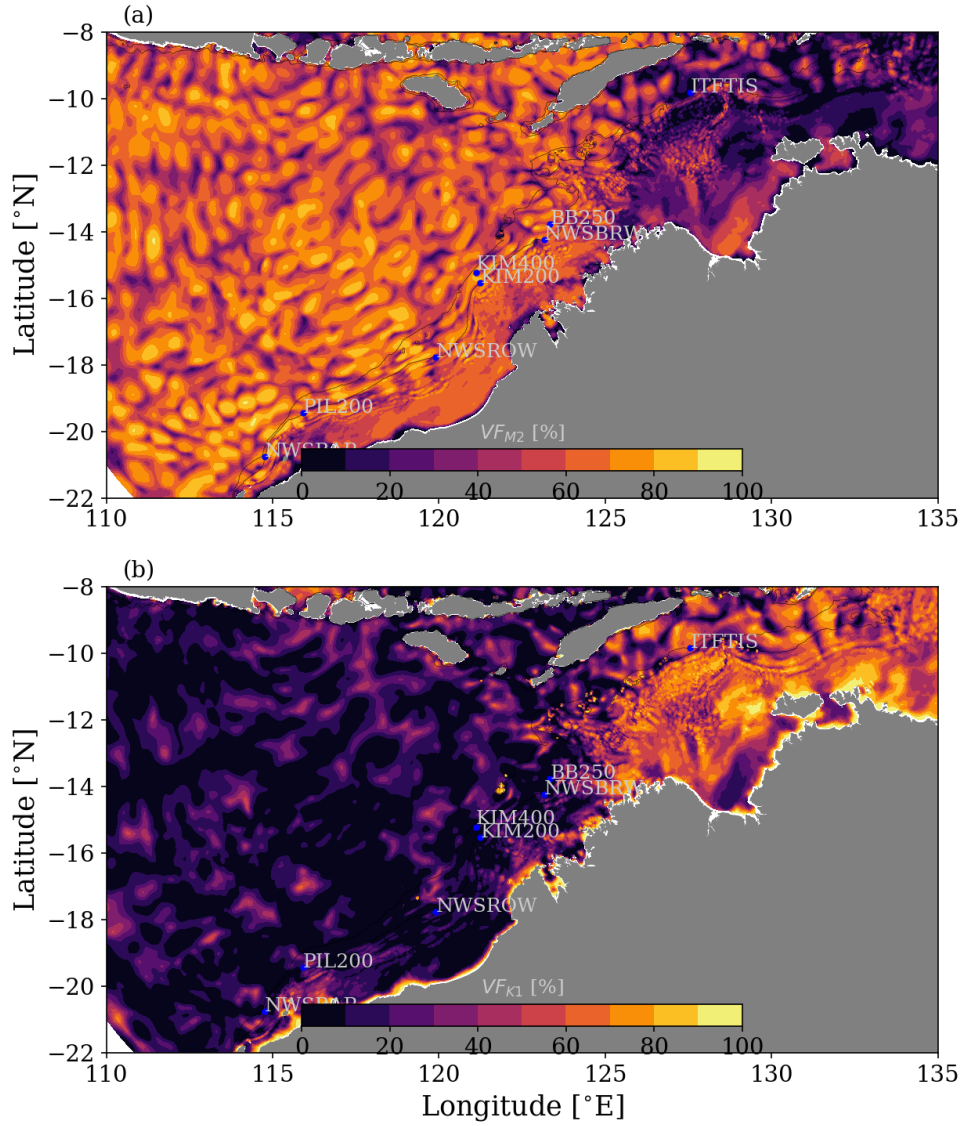


**Figure 9.** Percentage of variance of the SUTANS baroclinic SSH ( $VF_m$ , Eq. 9) explained by the (a)  $M_2$  and (b)  $K_1$  band harmonics, i.e., including the non-stationary annual harmonics.

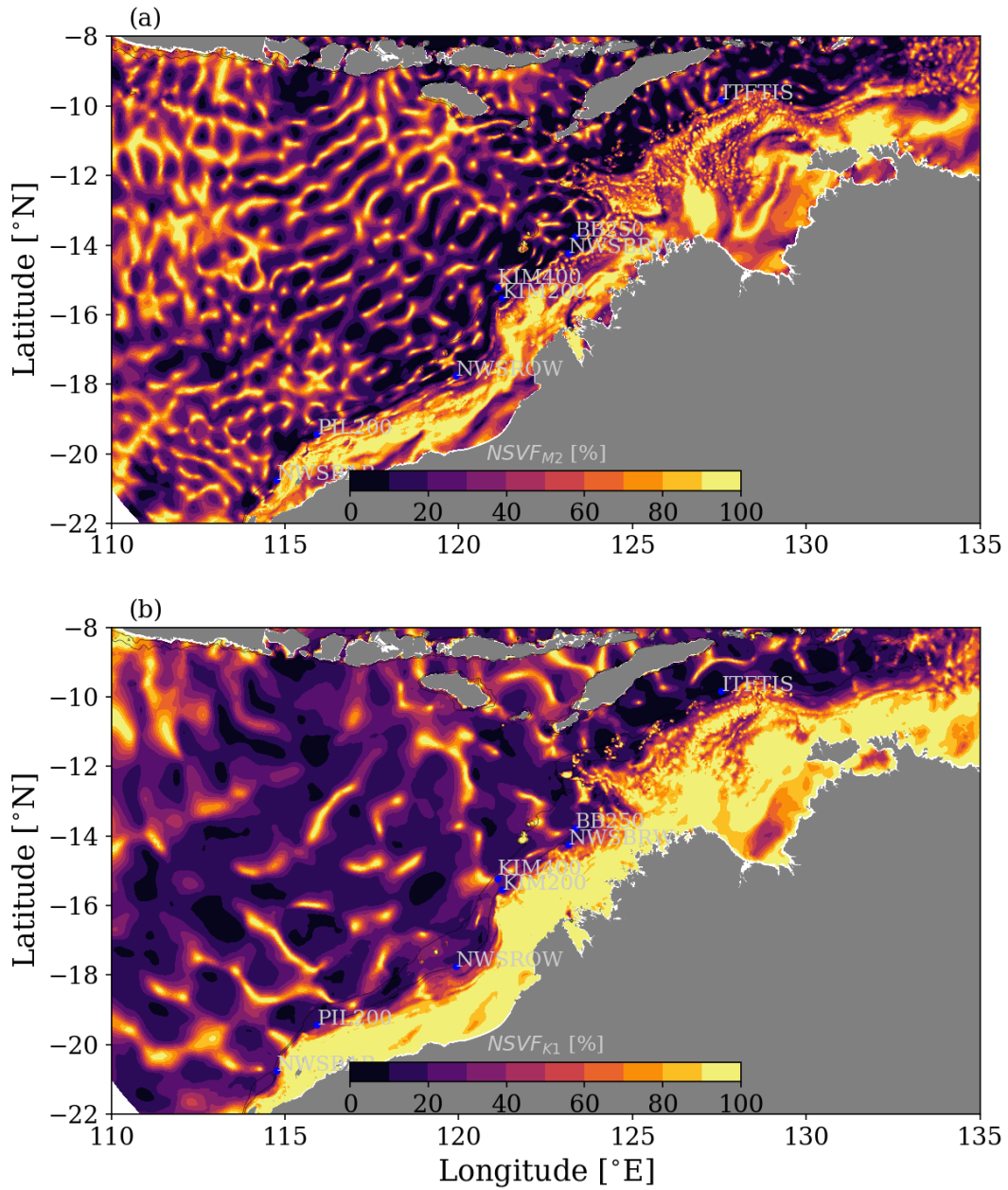


**Figure 10.** Percentage of variance of the SUNTANS baroclinic SSH ( $NSVF_m$ , Eq. 10) explained by the non-stationary harmonics in the (a)  $M_2$  and (b)  $K_1$  bands.

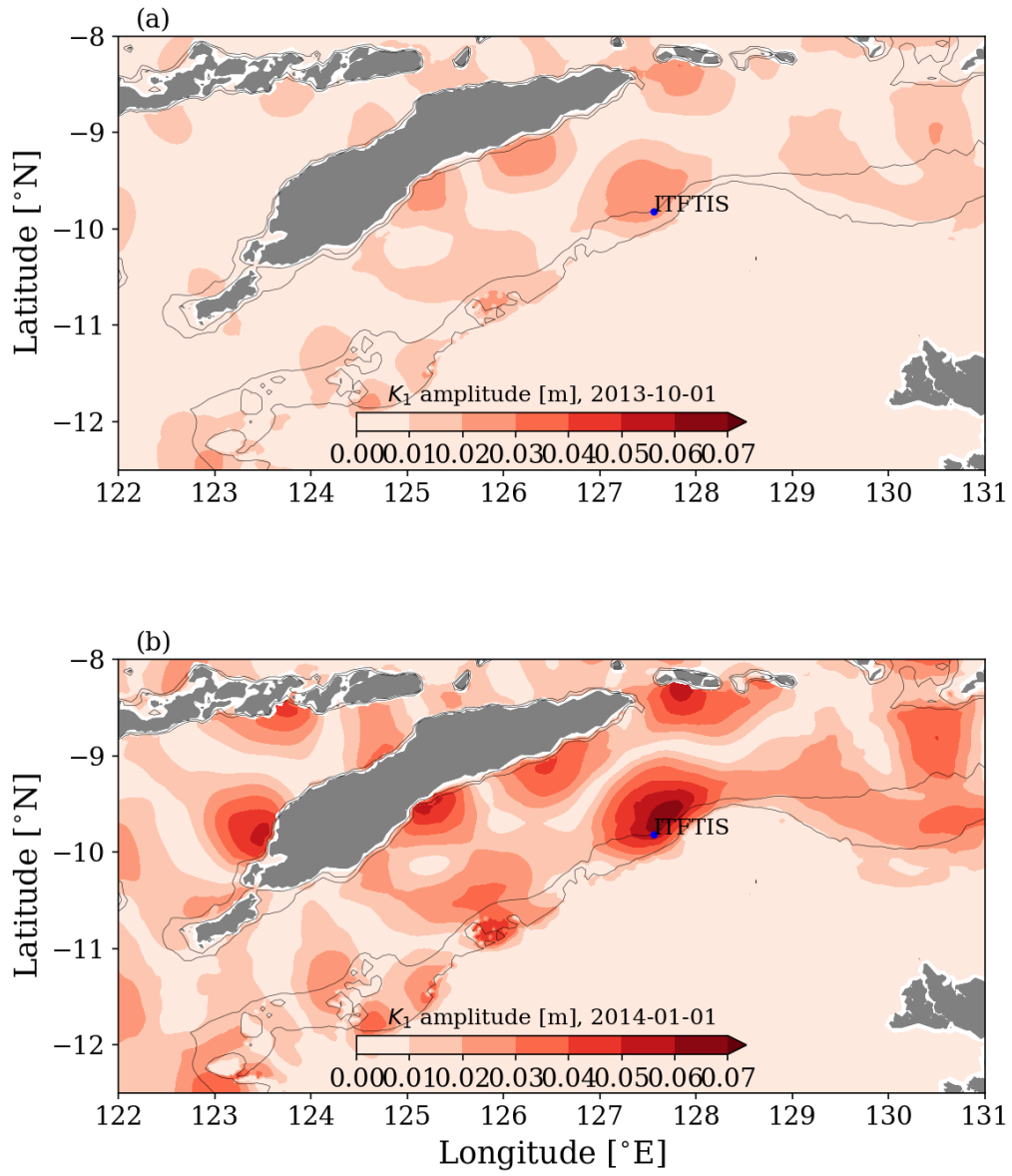


**Figure 11.** Snap-shots of  $|\eta_{K1}(t)|$  from the Timor Sea region during October and January.

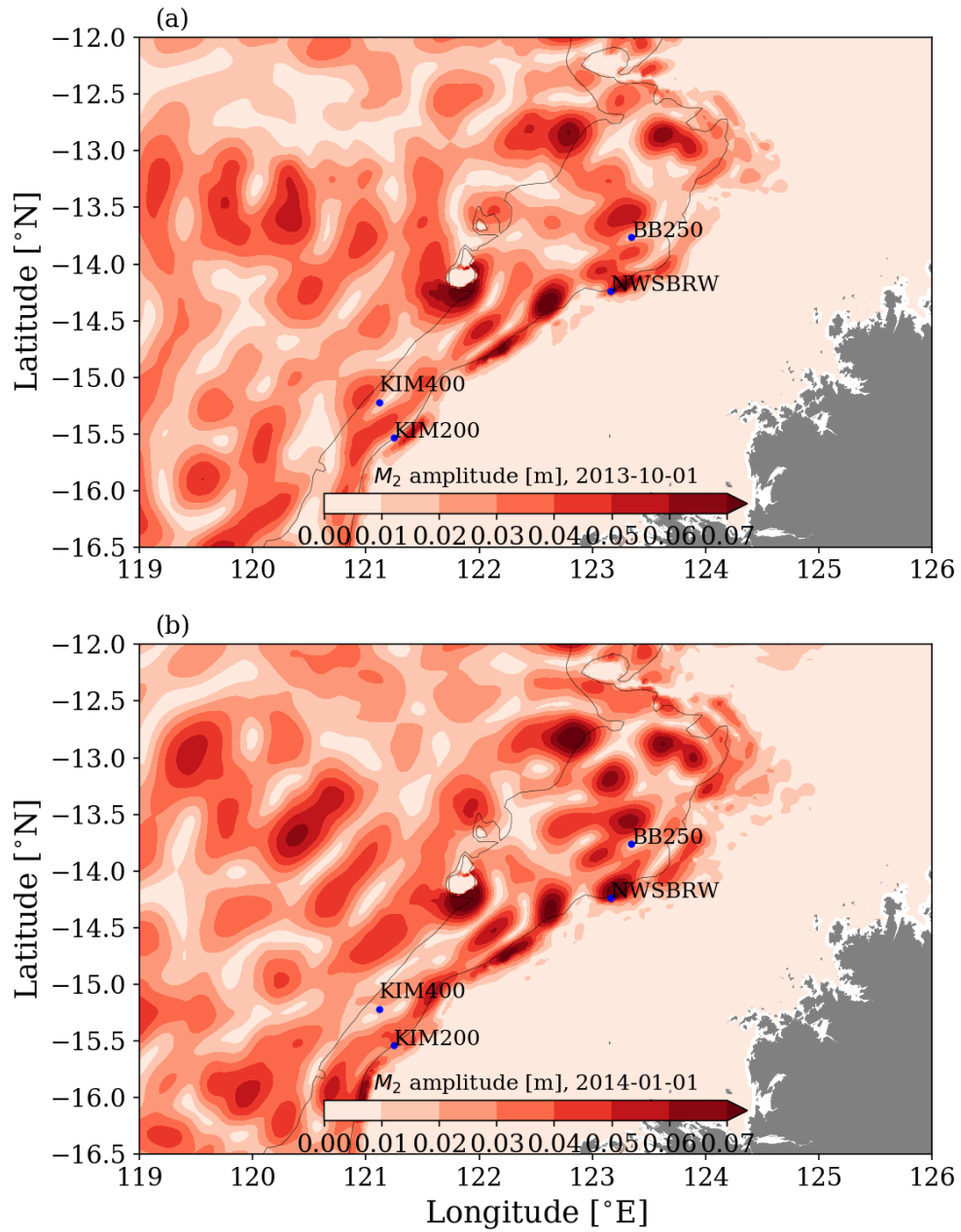


**Figure 12.** Snap-shots of  $|\eta_{M_2}(t)|$  from the Browse Basin region during October and January.

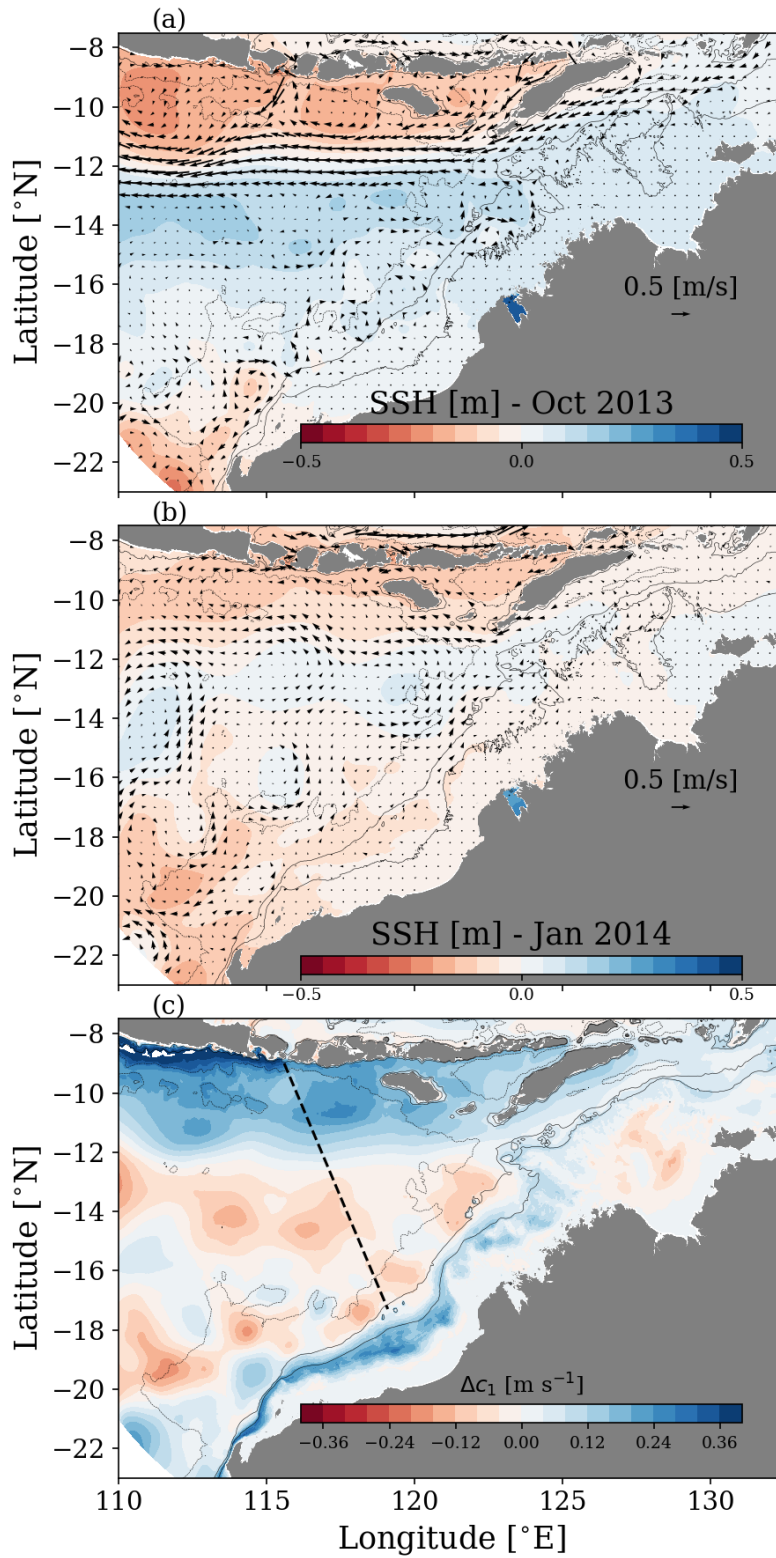


**Figure 13.** Monthly-averaged sea surface height (contours) and surface velocity (vectors) from the SUNTANS model for (a) October 2013 and (b) January 2014. The vector scale is indicated in the bottom right corner of each panel. (c) Indicates the mode-1 linear phase speed difference between the two months (January minus October).

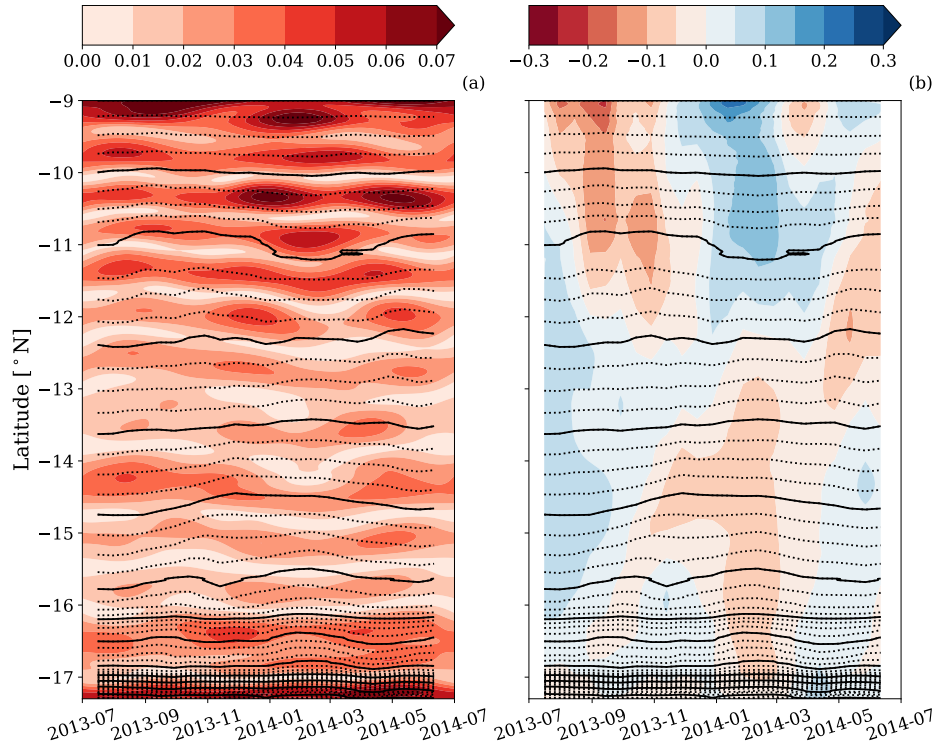


**Figure 14.** Temporal evolution of (a)  $|\eta_{M2}|$  [m] and (b) mode-1 phase speed anomaly [m/s] along the transect in Fig. 13c. Black contours indicate an estimate of the propagation time from the northernmost point in one cycle intervals (dotted contours indicate quarter cycle intervals).

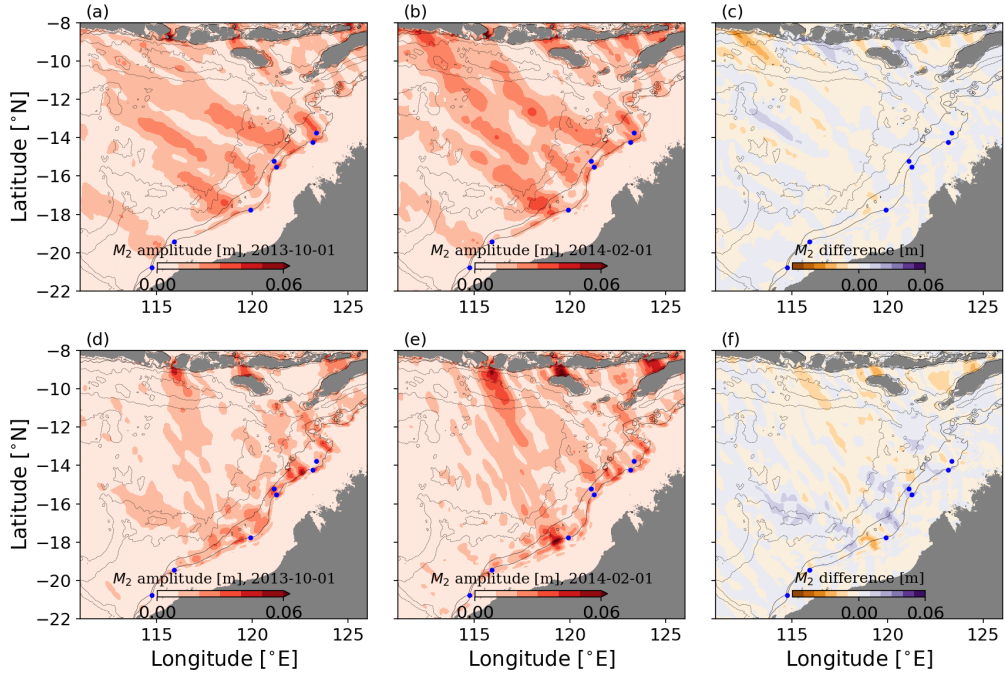


**Figure 15.** Directionally-decomposed internal tide sea surface height amplitude,  $\eta_{M_2}(t)$ , for (a, d) October 2013 and (b, e) February 2014. The top row indicates the NW propagating portion of the signal, whereas the bottom row indicates the SE component. The last column shows the difference between October and February for (c) the NW and (f) the SE component.

**Tables****Table 1.** Details of each in situ mooring used in this study to measure through-water-column temperature.

Site ID	Location	Water Depth [m]	Deployment Period	No. Instruments
ITFTIS	Timor Sea	460	2010 - 2019	17
KIM200	Kimberley	200	Mar 2012 - Aug 2014	14
KIM400	Kimberley	405	Mar 2012 - Aug 2014	17
PIL200	Pilbara	202	Mar 2012 - Aug 2014	14
NWSBAR	Barrow Island	200	Aug 2019 - Feb 2020	15
NWSROW	Rowley Shoals	200	Aug 2019 - Feb 2020	14
NWSBRW	Browse Island	200	Aug 2019 - Feb 2020	15

**Table 2.** Statistics of the internal tide amplitude at each mooring. Standard deviation (Std. Dev.) and percentage of total mode-1 internal wave amplitude signal variance explained by two different band-pass filters: the internal tide filter (6 - 34 hour cutoff period) and the internal tide, including nonlinear steepening (3 - 34 hour cutoff).

Site	Std. Dev. [m]	Percentage of Variance (%)	
		6 - 34 hour	3 - 34 hour
ITFTIS	7.3	52.2	75.8
KIM200	6.5	30.0	80.5
KIM400	3.5	25.5	69.4
PIL200	7.1	28.3	77.0

**Table 3.** Performance metrics of the stationary (stat., Eq. 1) and nonstationary (nonstat., Eq. 6) models at predicting mode-1 internal tide amplitude at each of the mooring locations.

Site	RMSE [m]	RMSE [m]	Skill	Skill
	Stat.	Nonstat.	Stat.	Nonstat.
ITFTIS	4.35	3.52	0.66	0.78
KIM200	3.62	2.90	0.70	0.81
KIM400	2.66	2.32	0.43	0.57
PIL200	4.72	4.19	0.45	0.57

**Table 4.** Performance metrics of the stationary (stat., Eq. 1) and nonstationary (nonstat., Eq. 6) models at predicting the sea surface height perturbation at each of the mooring locations for the period July 2013 - July 2014.

Site	RMSE [cm]	RMSE [cm]	Skill	Skill
	Stat.	Nonstat.	Stat.	Nonstat.
ITFTIS	2.11	1.57	0.78	0.88
KIM200	1.91	1.6	0.56	0.69
KIM400	1.23	1.11	0.27	0.41
PIL200	2.41	2.14	0.30	0.45

**Table 5.** Performance metrics of the stationary (stat., Eq. 1) and nonstationary (nonstat., Eq. 6) models at predicting sea surface height perturbation at each of the mooring locations for the period when data was withheld (July 2012 - July 2013).

Site	RMSE [cm]	RMSE [cm]	Skill	Skill
	Stat.	Nonstat.	Stat.	Nonstat.
ITFTIS	2.15	2.13	0.75	0.76
KIM200	2.13	2.16	0.46	0.45
KIM400	1.38	1.41	0.12	0.08
PIL200	3.08	3.04	0.16	0.18

**Table 6.** Validation metrics for the SUNTANS-derived  $SSH_{BC}$  from Eq. 6 compared against in situ observations.

Site	Dates	RMSE [cm]	Skill
ITFTIS	July 2013- Jun 2014	3.25	0.47
KIM200	July 2013- Jun 2014	2.29	0.37
KIM400	July 2013- Jun 2014	1.82	-0.60
PIL200	July 2013- Jun 2014	2.85	0.02
NWSBAR	Aug 2019 - Feb 2020	4.58	0.12
NWSROW	Aug 2019 - Feb 2020	2.86	0.45
NWSBRW	Aug 2019 - Feb 2020	5.80	0.67

**Table 7.** Description of different tidal harmonic metrics from the SUNTANS model at each in situ observation site.

Site	TVFH	SVFH	VF_M2	VF_K1	NSVF_M2	NSVF_K1
ITFTIS	94.7	87.2	2.1	61.8	40.3	9.5
KIM200	68.0	54.3	54.6	9.9	20.7	30.5
KIM400	49.7	28.5	67.2	6.8	40.4	36.4
PIL200	61.7	35.5	43.2	23.8	59.1	16.4
NWSBAR	68.4	58.3	76.9	11.9	10.4	23.2
NWSROW	75.7	62.8	36.6	8.0	14.0	28.1
NWSBRW	94.5	89.7	56.9	2.9	2.1	15.4

# Supporting Information for "A non-stationary harmonic model for seasonal internal tide amplitude prediction"

M. D. Rayson, N. L. Jones, G. N. Ivey, Y. Gong

<sup>1</sup>Oceans Graduate School and the Oceans Institute, University of Western Australia

## Contents of this file

1. Text S1 to S3
2. Figures S1 to S3

**Introduction** This supporting material shows additional SUNTANS versus mooring water temperature validation plots for three additional sites (KIM400, KIM200, PIL200).

---

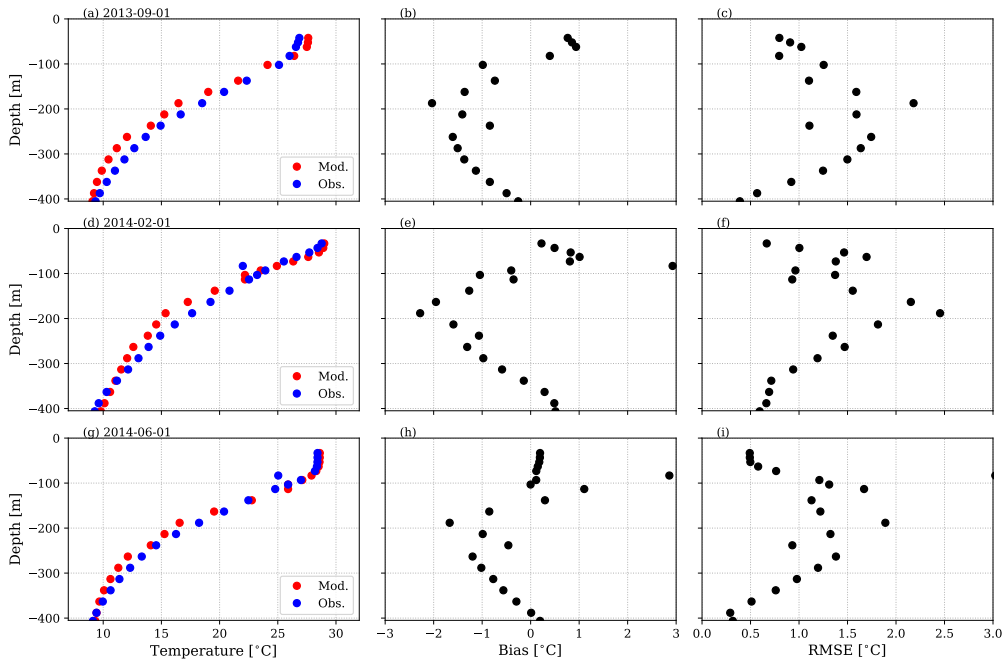


**Figure S1.** Quantitative SUNTANS model evaluation metrics against in situ temperature observations from the KIM400 mooring of (left column) monthly-averaged temperature, (middle column) temperature bias, and (right column) temperature root mean square error. Each row corresponds with monthly-averages for September 2013, February 2014 and June 2014.

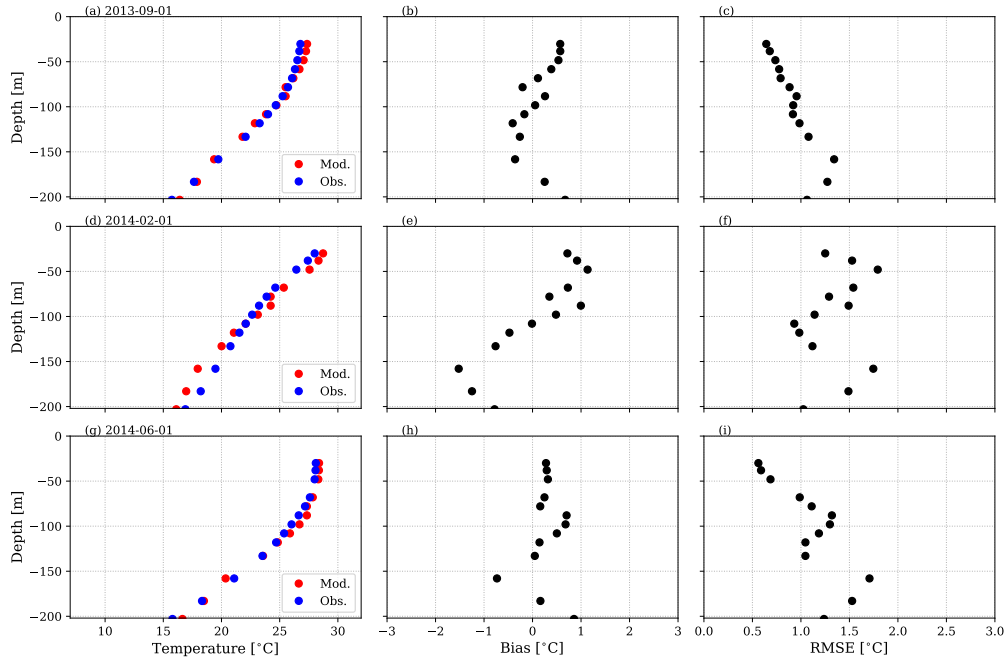


**Figure S2.** As in Fig. S1 but for the KIM200 mooring.

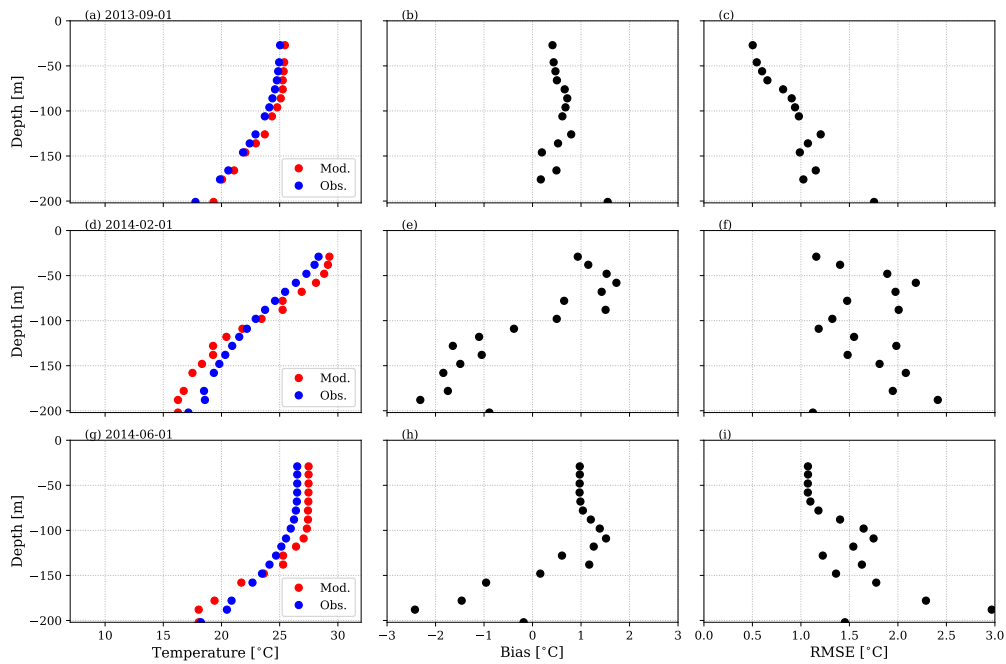


**Figure S3.** As in Fig. S1 but for the PIL200 mooring.